

Peak-ring magnetism: Rock and mineral magnetic properties of the Chicxulub impact crater

Bruno Daniel Leite Mendes^{1,†}, Agnes Kontny¹, Michael Poelchau², Lennart A. Fischer², Ksenia Gaus¹, Katarzyna Dudzisz³, Bonny W.M. Kuipers⁴, and Mark J. Dekkers⁵

¹*Institute of Applied Geosciences—Structural Geology and Tectonics, Karlsruhe Institute of Technology, 76131 Karlsruhe, Germany*

²*General Geology and Structural Geology, Albert Ludwig University of Freiburg, 79085 Freiburg, Germany*

³*Institute of Geophysics, Polish Academy of Sciences, PL01452 Warsaw, Poland*

⁴*Debye Institute for Nanomaterials Science, Utrecht University, 3584 CC Utrecht, Netherlands*

⁵*Paleomagnetic Laboratory Fort Hoofddijk, Department of Earth Sciences, Utrecht University, 3584 CD Utrecht, Netherlands*

ABSTRACT

The Chicxulub impact event at ca. 66 Ma left in its wake the only complex crater on Earth with a preserved peak ring, characterized by a well-developed magnetic anomaly low. To date, little is known about its magnetic properties. The joint Integrated Ocean Drilling Program (IODP) and International Continental Scientific Drilling Program (ICDP) Expedition 364 drill core M0077A revealed that the peak ring consists of uplifted and strongly deformed granitoid basement rocks overlain by a 130-m-thick impact melt and suevite layer. Pre- and postimpact hydrothermal systems affected this basement with maximum temperatures up to 450 °C. We used microscopy, mineral chemistry, temperature-dependent magnetic susceptibility, and hysteresis properties to characterize the magnetic mineralogy of pre-, syn-, and postimpact rocks. Compared to its amount of pure, stoichiometric shocked magnetite, the granitoid basement shows low magnetic susceptibility, which is in line with earlier experimental studies indicating that shock reduces magnetic susceptibility. Cation-substituted magnetite with varying compositions in the melt rocks carries a higher induced and remanent magnetization compared to the basement. In the granitoid basement, magnetite was partially oxidized to hematite by a pre-impact hydrothermal event, but at lithological contacts with high-temperature impact melt rock, this hematite was locally retransformed back to magnetite. Elsewhere in the granitoid basement, the temperature reached in the hydrothermal system was too

low for hematite retransformation. It was also too low to anneal all the lattice defects in the shocked magnetite, which likely occurs above 540 °C. The presence of shocked magnetite in the granitoid basement well explains the magnetic anomaly low due to its unusually low induced magnetization.

INTRODUCTION

The Chicxulub impact event marked the end of the Mesozoic Era, and it is widely regarded as a main contributor to the Cretaceous–Paleogene extinction event of the nonavian dinosaurs and to severe global environmental changes (e.g., Hildebrand et al., 1991; Sharpton et al., 1992; Smit, 1999; Schulte et al., 2010). It was the last of the “Big Five” Phanerozoic mass extinctions, and the impact left the third largest impact crater known on Earth (e.g., Witts et al., 2018; Burgess, 2019). The impact took place in the Yucatán Peninsula, Mexico (Fig. 1A), at ca. 66 Ma (e.g., Renne, 2013) by the collision of an asteroid of carbonate chondrite composition ~12 km in diameter hitting Earth with a steeply inclined trajectory from the NE (Collins et al., 2020).

The size of the impactor caused the formation of a complex impact crater ~200 km in diameter. Due to the interaction of the outward-collapsing central uplift and inward-collapsing transient wall (e.g., Riller et al., 2018), a so-called peak ring ~150 km in diameter was formed showing a characteristic magnetic anomaly (Fig. 1B) and a noteworthy gravity signature (Fig. 1C). The Chicxulub structure is the only known complex impact crater on Earth that preserved its peak ring (e.g., Morgan et al., 2000), largely due to an ~1-km-thick Cenozoic sediment cover in the Gulf of Mexico (Fig. 1A). Another special feature of the Chicxulub impact crater is the

existence of a postimpact, well-developed and long-lived (0.5 up to 2 m.y.) hydrothermal system, with fluid temperatures of 350 °C to 450 °C (Kring et al., 2020).

To date, myriad scientific and exploration drilling projects have been carried out, making the Chicxulub structure one of the best investigated impact craters on Earth (e.g., Burgess, 2019). However, only core M0077A from the joint Integrated Ocean Drilling Program (IODP) and International Continental Scientific Drilling Program (ICDP) Expedition 364 (Morgan et al., 2017) ever drilled and recovered samples from the Carboniferous granitoid basement at the peak ring of the crater (Zhao et al., 2020; Ross et al., 2022). This core was drilled through the melt-bearing polymict impact breccia (suevite), upper impact melt layer, and through the shocked granitoid basement, down to a depth of 1334.69 m below seafloor (mbsf). The recovery of this wide range of crater lithologies provides a unique opportunity for research into the rock and paleomagnetic properties that carry the magnetization and are responsible for the characteristic circular high-amplitude aeromagnetic anomalies (Fig. 1B).

Paleomagnetic research on drill core M0077A has been conducted in previous works to investigate the polarity of the peak ring through natural remanent magnetization (NRM) vector inclinations (e.g., Tikoo et al., 2017; Kring et al., 2020). These works determined reverse polarities in samples from the impact melt unit, with inclinations of ~−44° expected for the impact location during chron 29r. Zones of normal polarity in the upper peak-ring suevite unit have been interpreted as chemical remanence from secondarily deposited (Ti-)magnetite formed during postimpact hydrothermal activity at sufficiently elevated temperatures (100 °C to 250 °C; Kring

[†]bruno.mendes@kit.edu

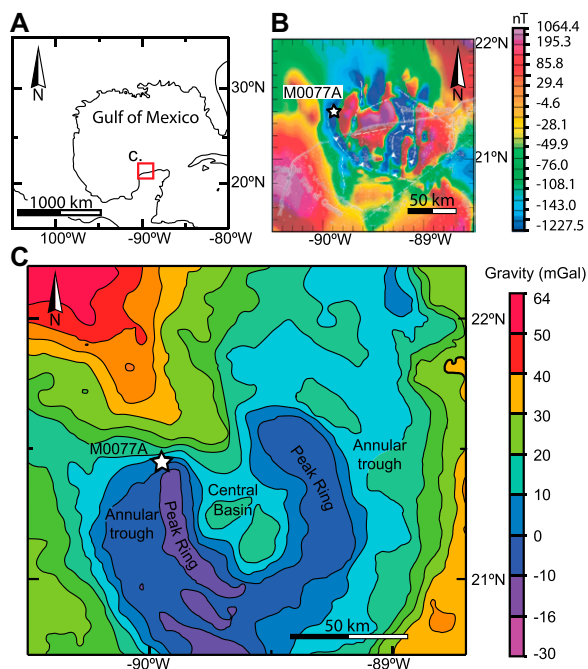


Figure 1. (A) Geographic location of the Chicxulub impact crater (red box) in the Yucatán Peninsula, Mexico. (B) Aeromagnetic anomaly map (nT) (after Rebolledo-Vieyra et al., 2010). (C) Gravity anomaly map (mGal) (modified after Gulick et al., 2013), with location of borehole M0077A indicated with a white star in a magnetic and gravity low corresponding to the peak ring.

et al., 2020). Other authors have argued that a wide variability of inclinations may suggest no postdepositional remagnetization, as temperatures would be too low (Gulick et al., 2019).

The magnetic anomaly above the Chicxulub impact crater was originally discovered in 1981 by Penfield and Camargo (1981), and it was crucial for the discovery and exploration of the impact crater (e.g., Hildebrand et al., 1991; Sharpton et al., 1992; Morgan et al., 1997; Gulick et al., 2008; Morgan and Artemieva, 2008). Melt rock, impact breccias, and the central uplift were interpreted as major magnetic sources for the composite character of the Chicxulub anomaly field, with large-amplitude inverse dipolar anomalies in the central sector (Rebolledo-Vieyra et al., 2010). Pilkington et al. (2004) reported that the predominant magnetic mineral in the drill core Yax-1 from the Chicxulub Scientific Drilling Project was secondary magnetite formed from low-temperature (<150 °C) hydrothermal alteration. However, exceptionally high magnetic susceptibilities are related to mafic basement gabbro clasts in the impact breccia (Pilkington et al., 2004). In drill core M0077A, rock magnetic measurements indicate high magnetic susceptibility in the impact melt-bearing lithologies and dikes and low magnetic susceptibilities in granitoid basement rocks (Fig. 2; Urrutia-Fucugauchi et al., 2018). Magnetite and titanomagnetite are described as main magnetic carriers (Kring et al., 2020; Urrutia-Fucugauchi et al., 2018), while secondary magnetite and Fe-sulfides are also reported as high-temperature (300–400 °C) alteration products (Kring et al.,

2017). The basement rocks are highly fractured with a high concentration of planar features and feather features in quartz (Riller et al., 2018), indicating average shock pressures in the range 10–35 GPa, and locally >60 GPa, as suggested by the occurrence of impact melt rock (Morgan et al., 2017; Ferrière et al., 2017). The extreme fracturing explains the very low density and high porosity of the drilled rocks, causing the gravity anomaly (Fig. 1C).

Although the principal structural elements of the magnetic anomaly pattern are thought to be largely understood, only direct sampling of one of the magnetized zones within the impact melt layers would provide conclusive information (e.g., Morgan et al., 2000; Pilkington et al., 2004; Rebolledo-Vieyra et al., 2010). Until now, it has remained unclear how the shocked basement rocks influence the magnetic anomaly pattern, although shock-related reduction of magnetic susceptibility is a well-known phenomenon (e.g., Acuña et al., 1999; Plado et al., 1999; Pilkington and Hildebrand, 2000; Ugalde et al., 2005; Reznik et al., 2016; Kontny and Grothaus, 2017). In experimentally shocked multidomain (MD) magnetite, the mass-specific bulk susceptibility decreases exponentially by ~90% for pressures up to 10 GPa (Reznik et al., 2016). Similar results have also been found for experimentally shocked pyrrhotite by Louzada et al. (2010) and Mang et al. (2013). Particularly in the low shock pressure range below 10 GPa, this seems to be a general shock-related phenomenon of magnetic material. The main reasons for these changes are magnetic domain size reduc-

tion (Reznik et al., 2016) and alteration of ferromagnetic phases (e.g., Kontny and Grothaus, 2017). Recent investigations of shocked minerals suggested that postshock thermal exposure may lead to a recovery of some of these preshock properties through thermal annealing (Kontny et al., 2018).

The M0077A drill core is the first core probing into the uplifted shocked basement and provides a unique opportunity to study the multiple lithological contributors to the anomalous magnetic field (Fig. 1B). We investigated the rock-magnetic properties and magnetic mineralogy of the impact and shocked basement rocks from the Chicxulub peak ring in order to better understand impact-related modifications of magnetic properties. To this end, we analyzed 44 samples from drill core M0077A to distinguish pre-, syn-, and postimpact magnetite in these lithologies. We also evaluated the shock and postshock thermal overprint, either due to the remaining heat during cooling of the impact melt rocks, or due to postimpact hydrothermal temperature overprinting. This knowledge can be used to better understand the Chicxulub crater magnetic anomaly pattern.

GEOLOGIC SETTING AND SAMPLES

Lithology of Core M0077A in the Chicxulub Peak Ring

The Chicxulub impact structure is located in the northwest part of the Yucatán Peninsula, Mexico (Fig. 1A). Here, the peninsula is composed of an ~3-km-thick Lower Cretaceous carbonate platform sequence composed of limestone, dolomite, marl, and anhydrite (e.g., Ramos, 1975; Gulick et al., 2008). It overlies the crystalline Maya block, which is mainly composed of Pan-African rocks (e.g., Keppie et al., 2011; Weber et al., 2018). The cored granitoid rock of the Chicxulub peak ring intruded the Maya block during Carboniferous times in an arc setting with crustal melting related to the closure of the Rheic Ocean (Feignon et al., 2021). Rasmussen et al. (2019) and Ross et al. (2022) determined U-Pb zircon ages between 334 and 326 Ma.

A total core length of 1334.69 mbsf was recovered during IODP-ICDP Expedition 364 at Site M0077A in 2015 (Morgan et al., 2017). The lithologies of the peak ring can be subdivided into four general units (Fig. 2; Morgan et al., 2017). Unit 1 is composed of postimpact Paleogene to Quaternary carbonate rocks, units 2 and 3 are impactite rocks, syngenetically formed during the impact event, and unit 4 represents Carboniferous basement granitoid rock, which is intruded by impact and pre-impact dikes.

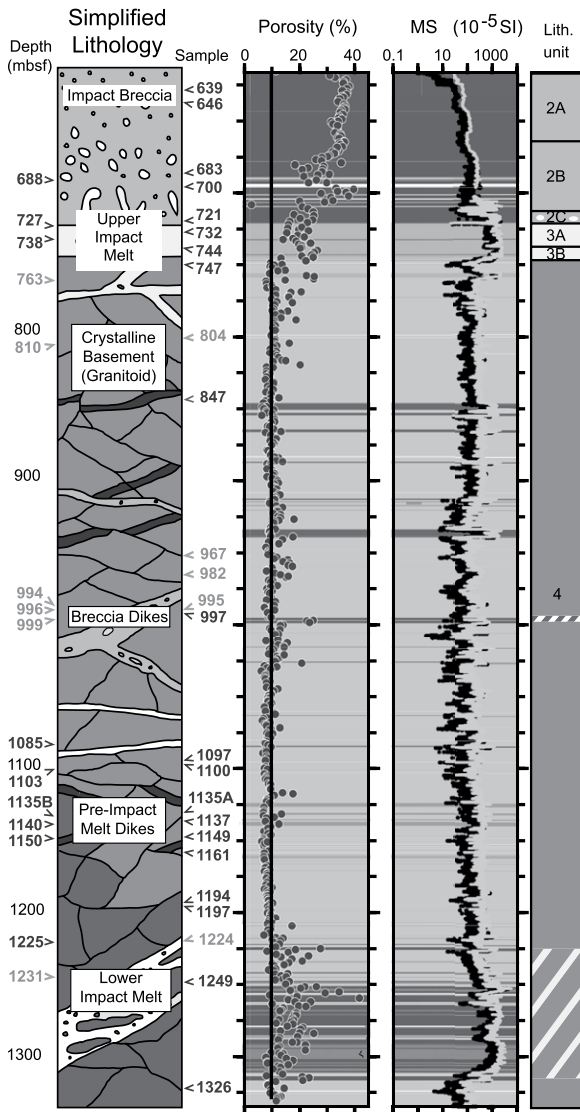


Figure 2. Simplified lithological units (Lith. unit) of borehole M0077A, as well as downhole porosity and magnetic susceptibility (MS) data (modified after Gulick et al., 2017a). Black dots correspond to multisensor core logger (MSCL) measurements, while gray line represents the downhole log measurements. Sample code corresponds to its approximate depth in meters below seafloor (mbsf). Samples in black represent samples taken with the onshore science party for Expedition 364 in Bremen (Germany) by M.P., while samples in gray were provided by the Gulf Coast Repository of the International Ocean Discovery Program (IODP), College Station, Texas (USA). Lithological units: unit 2 (A, B, and C)—suevite; unit 3 (A and B)—upper impact melt; unit 4—basement granitoid (lighter intersections are lower impact melt dikes).

rence of basement granitoid clasts. It is in direct contact with the impact melt of unit 3. Unit 2C is a coarse-grained, poorly sorted suevite, and the first impact breccia to be deposited after the impact. During deposition, this suevite probably maintained temperatures above 580 °C, the Curie temperature of pure magnetite (de Graaff et al., 2022). This unit was later exposed to explosive meltwater interactions from the tidal resurge that deposited units 2A and 2B shortly afterward (Gulick et al., 2019; Osinski et al., 2020). It also shows the highest magnetic susceptibility, increasing progressively from the top of the unit (100×10^{-5} SI) to the basal contact with the melt rock of unit 3 (1000×10^{-5} SI). This subunit shows the lowest porosity values of the suevites (20%–30%), values which are comparable with the melt (unit 3). Units 2C and 3 record a thermal remanent magnetization with inclination around -46° , while units 2A and 2B show highly scattered (negative and positive) magnetic inclination values (Gulick et al., 2019; Kring et al., 2020).

Unit 3

Unit 3 (721.61–747.02 mbsf) comprises an ~26-m-thick impact melt layer, subdivided into two subunits of different melt compositions: a calcium-rich green schlieren and black impact melt mixture (unit 3A, 721.61–737.56 mbsf) followed downward by a continuous section of silica-rich black melt rock (unit 3B, 737.56–747.02 mbsf). At the transition between units 3A and 3B, the green schlieren disappears, although a similar calcium concentration for both subunits is reported (de Graaff et al., 2022). There are also no differences between subunits concerning porosity (20%–30%) or magnetic susceptibility ($\sim 1000 \times 10^{-5}$ SI); both are similar to unit 2C. The upper boundary of unit 3A is a gradual transition from the coarse-grained breccia of unit 2C, and its lower boundary is characterized by the complete disappearance of the green schlieren. The disappearance of green schlieren occurs gradually, with intense brecciation at the top, via mingling of calcium- (similar to carbonate melts) and silica-rich melts, to a complete mixing of the two melts in unit 3B (Osinski et al., 2020; de Graaff et al., 2022). Unit 3B is characterized by the black SiO_2 -rich melt containing shocked basement clasts (Gulick et al., 2019). Melt temperatures of unit 3 have been constrained to be potentially between ~ 650 °C and ~ 750 °C (de Graaff et al., 2022). We refer to the whole unit 3 as upper impact melt.

Unit 4

Unit 4 (747.02–1334.69 mbsf) consists of the shocked felsic granitoid basement. This is a coarse-grained granite, with pre-impact mag-

As our study investigated the relation between temperature and shock and its influence on the magnetic mineralogy in the impact lithologies and basement granitoids, the postshock carbonate platform sedimentary rocks of unit 1 are not considered further.

Unit 2

Unit 2 (617.33–721.61 mbsf) comprises a sequence of melt-bearing suevite layers. Clast sizes decrease from bottom to top (e.g., Gulick et al., 2017b, 2019). This unit is very porous ($\sim 15\%$ – 40%) and shows a generally low magnetic susceptibility (~ 10 – 100×10^{-5} SI; Fig. 2). The suevite can be subdivided into three subunits from top to bottom:

Units 2A (617.33–664.52 mbsf) and 2B (664.52–712.84 mbsf) are resurge sequences of breccia deposited at low temperatures, subse-

quent to crater flooding (Gulick et al., 2019). The distinction between units 2A and 2B is based on the amount of groundmass versus clasts, grain size, and the presence of sedimentary features: While unit 2A presents >20 repeated upward-coarsening or upward-fining structures and cross-lamination, unit 2B does not show any sedimentary structures besides a general upward-fining succession (Gulick et al., 2017b). Unit 2A shows a downhole increase of magnetic susceptibility from $\sim 10 \times 10^{-5}$ to 100×10^{-5} SI. This trend corresponds to a decrease in porosity from around 40% to 30% (Gulick et al., 2017b). In unit 2B, the porosity varies widely between 20% and 30%, while the magnetic susceptibility remains high, around 100×10^{-5} SI.

Unit 2C (712.84–721.61 mbsf) is a suevite sequence with black impact melt clasts in a gray and green matrix, with occasional occur-

matic dikes, as well as pegmatite and aplite dikes. This granite has been shocked at pressures from 10 to 35 GPa, and it shows (from a granite perspective) a high porosity of around 10%, with increased levels in the lower impact melt unit at the bottom. Also, its magnetic susceptibility is generally low: $10\text{--}300 \times 10^{-5}$ SI (Fig. 2). It is suggested that the granite was affected by two distinct hydrothermal alteration events (Feignon et al., 2021): (1) a pre-impact hydrothermal metasomatic event presumably related to the breakup of the supercontinent Pangea ca. 273 ± 21 Ma, ~ 50 m.y. after the granite emplacement; and (2) postimpact-related hydrothermal activity (e.g., Kring et al., 2020).

Between 1206.98 and 1334.69 mbsf, a section of prevalent impact melt dikes occurs, including sections with tens of meters of continuous impact melt. Henceforth, this section is referred to as lower impact melt unit. Dikes belonging to this lower impact melt are also exposed at 917.17, 995.24, and 1063.52 mbsf. These dikes occur at different angles and imply heavy deformation of the granite around the contact (Riller et al., 2018).

The lower impact melt unit is broadly characterized as a brecciated impact melt rock, containing both impact melt rock clasts and different basement-derived material (de Graaff et al., 2022). The absence of calcium-rich melt suggests that this unit consists predominantly of crystalline basement melt, with no contribution from the carbonate-rich sedimentary target rocks. These impact melts are interpreted to have been injected into the basement during the compression and excavation stages of the cratering process, and they are suggested to be delamination surfaces within the crystalline basement, which accommodated deformation during peak-ring formation (Riller et al., 2018). The lower impact melt in general also shows a higher concentration of Al_2O_3 , MgO, and FeO when compared with the upper impact melt (de Graaff et al., 2022).

After impact, the latent heat from the cooling of the impact melt helped to start and fuel a long-lived ($\sim 0.5\text{--}2.1$ m.y.) and hot ($350\text{--}450\text{ }^\circ\text{C}$) hydrothermal system, which could have extended to depths of 5–6 km below the seafloor. All the units described above show ubiquitous hydrothermal alteration, including the deposition of secondary sulfide minerals (e.g., pyrite, chalcopyrite; Kring et al., 2020). These hydrothermal fluids are interpreted as originally pH neutral and undersaturated in Si, as quartz was wholly or partially dissolved in the impact melt rocks. However, they evolved over time toward more alkaline fluids, which promoted the precipitation of smectite and calcite. It is suggested that secondary (Ti-)magnetite grains precipitated

in relation to protracted hydrothermal activity (Kring et al., 2020).

METHODS

Material

In total, 44 half and quarter drill core samples from site M0077A were used for this study (sample codes in black and gray; see Fig. 2). All sample names refer to approximate depth in meters below seafloor, but we omit the “mbsf” in the following sample names for better readability. Further, we give the sample unit in parentheses to help the reader contextualize its provenance. From 15 “black” samples, cylindrical specimens with 1.5 cm diameter and 1.2 cm length were stepwise demagnetized. We were able to reorient these cores using a computed tomography (CT) scan rotation log (after McCall et al., 2017; see Supplemental Text for details¹).

Sample 999 shows a contact between the shocked basement granite and an injection dike of the lower impact melt. The contact is a flow-foliated ultracataclastite between the granitoid rock and the lower impact melt, likely developed during peak-ring formation, where the melt dikes acted as deformation allocation zones (e.g., Riller et al., 2018; de Graaff et al., 2022). From this sample, we carefully cut six subsamples for temperature-dependent magnetic susceptibility (k - T) analysis, two from the basement, two from the melt, and two from the intermediate and contact region, in order to study the spatial

¹Supplemental Material. Supplemental Text is a descriptive document that contains information about the core correction procedure, additional hysteresis parameters vs. depth data, and a brief explanation of the remaining supplemental files. Supplemental Data S1 includes all electron probe microanalyzer (EPMA) data, including calibration parameters for the measurements. Highlighted samples are the samples selected for Table 1. Supplemental Data S2 contains all temperature-dependent magnetic susceptibility (k - T) data, including a table with all parameters, used for Table 2. Supplemental Data S3 contains all thermomagnetic curves (M - T) data, both raw data files and measurement graphs. Supplemental Data S4 contains all high-temperature annealing experiments shown in Figure 9. Note that only the data are presented; no graphs were plotted. Supplemental Data S5 is a spreadsheet with the calculations for Q ratios used in Figure 10. Supplemental Data S6 includes all hysteresis data, including pre- and postheating data, in individual measurement data files. Supplemental Data S7 contains all the paleomagnetic natural remanent magnetization (NRM) directional data. Supplemental Data S8 contains all isothermal remanent magnetization (IRM) component analysis data. Please visit <https://doi.org/10.1130/GSAB.S.22237114> to access the supplemental material, and contact editing@geosociety.org with any questions.

temperature overprint of the impact melt injections on the magnetic minerals. From sample 1100 (basement granite), we prepared a polished piece ~ 5 mm in diameter and subjected it to the same heat treatment as used during temperature-dependent magnetic susceptibility measurement (see Rock Magnetic Methods). This piece was observed under the microscope before and after heat treatment to investigate potential alteration of the magnetic phases due to temperature.

Microscopic and Mineral Chemical Analysis

We performed transmitted and reflected light microscopy with a Leitz polarizing microscope at the Karlsruhe Institute of Technology (KIT). In total, 64 electron probe microanalyses (EPMA) of magnetite and backscattered electron (BSE) images were obtained on 10 representative carbon-coated samples (Supplemental Data S1) at the University of Freiburg, Germany, using a Cameca SX100 electron microprobe with five wavelength-dispersive (WD) spectrometers and an energy-dispersive (ED) detector, with 15 nA current and 15 kV voltage settings. We used natural and synthetic standards for calibration of Cr, Si, Mg, Fe, Al, Ti, Ni, Mn, and Na (for details, see Supplemental Text and Supplemental Data S1) and calculated the spinel formula assuming a composition of three cations and four oxygens.

Rock Magnetic Methods

Rock magnetic investigations included temperature-dependent magnetic susceptibility (k - T), thermomagnetic curves (M - T), isothermal remanent magnetization (IRM) component modeling, and hysteresis loop analysis, as well as two first-order reversal curve (FORC) analyses for representative sample 1100 before and after heating. Temperature-dependent magnetic susceptibility analyses in a 300 A/m applied magnetic field were performed using an AGICO KLY-4S susceptometer (Brno, Czech Republic). The instrument was equipped with CS-L and CS-3 units, respectively, for low-temperature analysis (“LT,” from $-192\text{ }^\circ\text{C}$ to $15\text{ }^\circ\text{C}$) and high-temperature analysis (“HT,” from room temperature up to $700\text{ }^\circ\text{C}$; then cooled to $40\text{ }^\circ\text{C}$, at an average heating/cooling rate of $12\text{ }^\circ\text{C}/\text{min}$). LT curves were obtained by applying liquid nitrogen in the cryostat and cooling the sample down to $-192\text{ }^\circ\text{C}$ and letting it heat up through contact with ambient atmosphere, which causes heating rates to be faster at the beginning of the experiment. Temperatures were measured with a Pt resistance thermometer in contact with the samples. The accuracy of these thermometers is $\pm 1\text{ }^\circ\text{C}$ up to $150\text{ }^\circ\text{C}$ and $\pm 3\text{ }^\circ\text{C}$ from $150\text{ }^\circ\text{C}$ up

to 700 °C (Lattard et al., 2006). HT measurements were performed in a flowing argon atmosphere (110 mL/min, argon purity of 99.998%) in the furnace to minimize oxidation during analysis. However, it has to be mentioned that argon gas, even in high purity, can contain traces of gases like hydrocarbons (HCs; <https://industry.airliquide.us/argon>). We also measured some samples in ambient atmosphere to evaluate the influence of a different measurement environment. The k - T curves were compared with the temperature dependence of magnetization (M - T curves; see below).

Furthermore, we performed k - T experiments where crushed material from sample 1100 was annealed in an argon atmosphere subsequently at 450, 500, 520, 540, 560, and 580 °C, with intermittent cooling to room temperature. The reversibility of the samples was studied as we expected to observe a shock-pressure overprint in magnetite from the granitoid rocks (see, e.g., Reznik et al., 2016), and we also explored the temperature threshold at which annealing of the crystal lattice defects for magnetite occurs (Kontny et al., 2018).

Last, we performed repeated HT susceptibility experiments from room temperature up to 700 °C to investigate the stability of the magnetic phases after heating. We used two different crushed materials from sample 1100. The first was used for four consecutive repeated experiments with a standard heating/cooling rate of 12 °C/min. The second was used for two consecutive experiments with different heating rates: a first “slow” experiment (7 °C/min, with 20 min hold at maximum temperature), and a follow-up at the standard heating/cooling rate. Both sets of repeated experiments maintained a constant flowing argon atmosphere, and the samples were not exposed to air at any point during the process.

Hysteresis loop analyses were performed at the Debye Institute for Nanomaterials Research at Utrecht University (UU), Utrecht, Netherlands, using an EZ vibrating sample magnetometer (VSM) with a sensitivity of $\sim 5 \times 10^{-10}$ Am². This method provides insight into the mean coercivity and saturation magnetization behavior of the ferrimagnetic minerals. Sample shards (<20 mg) were glued to a Pyrex 8 mm transverse sample holder, and its position was adjusted for each individual measurement. These samples were then exposed to an applied field varying in field direction from 2.2 T to -2.2 T and back to 2.2 T, in a total of 110 data points. Between (\pm)2.2 T and (\pm)0.5 T, each step was 0.1 T, while within the 0.5 T to -0.5 T interval, each step was 0.01 T, for higher resolution. High field slope corrections were applied starting at 0.9 T. A second round of hysteresis measurements was done to investigate hysteresis property changes

postheating. We selected 20 samples from the upper impact melt (4 samples), lower impact melt (2 samples), and basement granitoid/lower impact melt dikes and contacts (14 samples) and performed HT k - T measurements in argon atmosphere, up to 600 °C, and repeated the hysteresis measurements. In addition to the hysteresis loops, the FORC of sample 1100 before and after heating was measured using an alternating gradient magnetometer (MicroMag AGM 2900, Princeton Measurement Corporation, Princeton, New Jersey). These measurements were done in steps of 2.0 mT, with an averaging time of 150 ms and a saturation field of 0.9 T. In total, 200 curves were measured and then processed, smoothed, and drawn using FORCINEL software (Harrison and Feinberg, 2008; Egli, 2013).

Isothermal remanent magnetization (IRM) was measured stepwise at room temperature by using a Micro-Mag 2900 AGM instrument (Princeton Measurements Corporation) with a maximum magnetic field of 1 T. At least 40 points were measured and further analyzed following the cumulative log-Gaussian functions for statistical analysis according to Kruijer et al. (2001). Three parameters describe the magnetic components obtained from the statistical analysis: saturated isothermal remanent magnetization (SIRM) proportional to the mineral content in the sample, the mean coercivity ($B_{1/2}$) at which half of the SIRM is reached, and the dispersion parameter (DP) corresponding to the individual cumulative log-normal distribution. Both, FORC and IRM measurements were done at the Institute of Geophysics, Polish Academy of Sciences in Warsaw, Poland.

The temperature dependence of magnetization (M - T) measurements were performed at the Fort Hoofddijk Paleomagnetic Laboratory (UU). For these measurements, we used a modified horizontal translation Curie balance (Mullender et al., 1993). We measured seven representative samples (two suevite samples, two melt rock samples, and three granitoid basement samples) in ambient atmosphere. The heating rate was 6 °C/min, the cooling rate was 10 °C/min, and peak temperatures of subsequent segments were: 150, 250, 350, 400, 450, 525, 620, and 700 °C.

Determination of Magnetic Transition Temperatures from k - T Curves

We determined the Verwey transition temperature (T_V) of magnetite using low-temperature k - T curves before and after the heating cycles (T_{V1} and T_{V2} , respectively; Fig. 3) by applying the first derivative method. In samples where this method was not possible, we used the tangent method as described by Lied et al. (2020). The Verwey transition temperature for pure stoichiometric

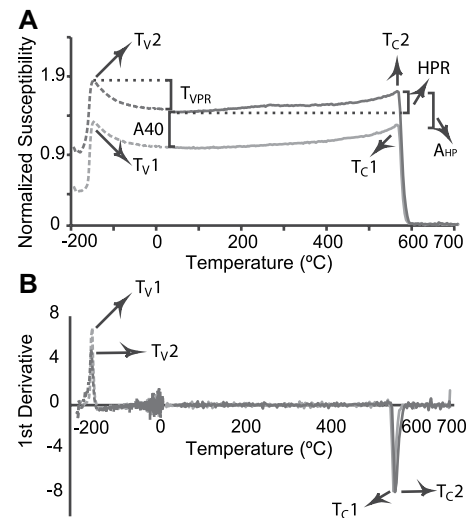


Figure 3. (A) Parameters from temperature-dependent magnetic susceptibility (k - T) that were used in this study. T_{V1}/T_{V2} —Verwey transition temperature pre- and postheating, respectively; T_{C1}/T_{C2} —Curie temperature of heating and cooling cycles, respectively; HPR —Hopkinson peak ratio; T_{VPR} —Verwey peak ratio; A_{40} [%]—alteration index at 40 °C; A_{HP} [%]—alteration index between Hopkinson peaks. (B) First derivative curve for k - T example, showing how T_C and T_V were identified (after Petrovský and Kapička, 2006).

magnetite is -153 °C (120 K; Verwey, 1939), and it is very sensitive to both lattice defects (i.e., due to shock; Reznik et al., 2016; Biało et al., 2019) and chemical inhomogeneities (i.e., cation substitution; Biało et al., 2019; or vacancy concentration; Aragón et al., 1985). With increasing numbers of lattice defects, the Verwey transition temperature tends to increase (Reznik et al., 2016), while cation doping and slight oxidation related to a higher number of vacancies cause a decrease in T_V , and its expression in k - T curves becomes less pronounced (Özdemir et al., 1993; Biało et al., 2019). T_V is also stress-sensitive and decreases when measured under pressure (e.g., Carporzen and Gilder, 2010) and increases upon pressure release (e.g., Reznik et al., 2016).

We identified the Curie temperatures (T_C) from the heating (T_{C1}) and cooling (T_{C2}) cycles (Fig. 3A) using the first derivative method (Fig. 3B; Petrovský and Kapička, 2006). This temperature defines the transition of ferromagnetic to paramagnetic behavior in magnetic minerals, and it allows the magnetic carriers to be identified. For pure magnetite, the Curie temperature is 578 °C. Lower values indicate cation substitution (e.g., Engelmann, 2008; Lattard et al., 2006), while oxidation of nonsubsti-

tuted magnetite forms as oxidized end-member maghemite ($\gamma\text{-Fe}_2\text{O}_3$) with a T_C up to 640 °C (e.g., Nishitani and Kono, 1981; O'Reilly, 1984; Özdemir and Dunlop, 2010).

We normalized both LT and HT k - T curves to the susceptibility values at room temperature, and the following parameters were used to evaluate the k - T curves:

(1) Verwey peak ratio: $T_{\text{VPR}} = k_{\text{max}}/k_{15}$, where k_{15} is the susceptibility value at 15 °C, and k_{max} is the maximum value around the Verwey transition (Kontny et al., 2018).

(2) Hopkinson Peak ratio: $\text{HPR} = k_{\text{max}}/K_{40}$, where K_{40} is the susceptibility value at 40 °C, and k_{max} is the maximum value before the Curie temperature (Dunlop, 2014).

According to Dunlop (2014) and Kontny et al. (2018), these ratios describe magnetic domain states and their changes during the heating experiments. In experimentally shocked magnetite, a decrease in peak ratios is associated with annealing of lattice defects and wall unpinning, leading to an increase of magnetic domain size (Kontny et al., 2018). A third useful parameter is:

(3) A_{40} parameter: $A_{40} [\%] = 100 \times [(k_{40} - K_{40})/K_{40}] \times 100$, where k_{40} and K_{40} are the susceptibility values at 40 °C in the cooling and heating branch, respectively (Hrouda, 2003).

This parameter characterizes the alteration of magnetite during k - T measurements. A positive A_{40} value indicates an increase of postheating susceptibility, suggesting the formation of a ferromagnetic phase, or relaxation of strain in the crystal lattice during the experiment; a negative A_{40} value indicates a decrease of susceptibility during heating due to mineral transformations to a phase with lower magnetic susceptibility (e.g., maghemite to hematite).

A fourth parameter was used to quantify the formation of new magnetite across the Curie temperature:

(4) A_{HP} parameter: $A_{\text{HP}} [\%] = 100 \times [(k_{\text{HP}} - K_{\text{HP}})/K_{\text{HP}}] \times 100$, where k_{HP} and K_{HP} are the susceptibility values at the Hopkinson peak in the cooling and heating branch, respectively (Fig. 3).

This parameter is similar to A_{40} , as it characterizes the irreversible alteration of magnetite, but here we used it to control the formation of new magnetite during heating in the HT annealing experiments. If this parameter is distinctly positive, it suggests the formation of new magnetite in the sample during heating.

Paleomagnetic Directional Analysis

We obtained paleomagnetic directions for 25 specimens with an AGICO JR5A spinner magnetometer, controlled by AGICO's Remasoft 3.0 (Chadima and Hrouda, 2007). Both thermal and alternating field (AF) stepwise demagnetiza-

tion experiments were performed on duplicate samples from the same core piece. Thermal demagnetization was performed with 40–60 °C steps from room temperature up to 750 °C with a Magnetic Measurements (UK) thermal demagnetizer (MMTD1). AF demagnetization was performed using a Magnon International (MI) AFD 1.1 demagnetizer in 12 steps of 2.5–30 mT, up to 160 mT. All measurements and demagnetization were performed in a low-field environment inside an in-house-built low-field Faraday cage. We calculated the magnetic component directions from Zijderfeld diagrams (Zijderfeld, 1967) through principal component analysis (Kirschvink, 1980) and the composite great circle approach described in McFadden and McElhinny (1988). For the upper impact melt and suevite data, a 45° cutoff angle around the average direction was applied, excluding one sample. Interpretation of the data was done using the platform Paleomagnetism.org (Koymans et al., 2016, 2020).

RESULTS

Texture and Composition of Magnetic Phases

Granitoid Basement

The main magnetic phase in the shocked granitoid basement is magnetite, which shows grain sizes of ~ 100 μm up to ~ 500 μm . These grains are often strongly fractured and show corroded rims (Figs. 4A and 4B), often with sulfide fillings in cracks. Ubiquitous oxidation to hematite was noted as well (Fig. 4B).

Some of the intragranular fractures do not extend to the surrounding quartz and feldspar, and they often form shear fractures (see white lines in Fig. 4A). Smaller, irregular fractures often cause further fragmentation of magnetite into smaller grains between the main sets of cracks (Figs. 4A and 4B). The secondary hematite shows the same fracture patterns as the magnetite and thus predates the impact event. Smaller (10–50 μm) magnetite grains were also observed along fractures in the granitoid. EPMA results indicated that the shocked basement magnetite is generally pure (Table 1, where samples 747 and 1135 are representative of basement magnetite). These results are consistent throughout the basement and common to all of our granitoid samples.

Suevite

In suevite, visible magnetic phases are scarce and mostly occur in basement clasts, with the same characteristics as described in the granitoid. In the matrix, scarce, relatively small (< 10 μm), idiomorphic, nonfractured grains occur

(Fig. 4C), with most grains generally too small for EPMA analysis (spot size of 2–3 μm). The grains big enough to be measured showed a non-substituted (henceforth referred to as “pure”) magnetite composition (samples 646 and 721 in Table 1).

Upper Impact Melt

The composition of magnetite in the upper impact melt is not homogeneous throughout the profile. In the green schlieren samples of unit 3A, scarce clusters of magnetite with skeletal textures occur (clusters reach up to 50 μm , with individual grains often < 10 μm ; Fig. 4D). These clusters often contain sulfides, pyrite, and chalcopyrite, alongside the inverse spinel-group phases. Sulfides are prevalent throughout the impact melt units. Magnetite compositions vary between the uppermost (Table 1, sample 727) and lowermost parts (sample 732) of the upper impact melt, with some of the inverse spinel-group minerals ranging from a Ti-, Al-, and Mg-substituted magnetite (sample 727 points 2-1 and 2-2) to nearly pure magnetite (sample 732 point 3-11).

A wide variation of Ti-substitution in the oxides is shown by the Ti# (a number that quantifies the ratio between the titanium content and the remaining cations, given by $100 \times [2\text{Ti}/\{2\text{Ti} + \text{Al} + \text{Cr}\}]$; see Fig. 5). In the titanomagnetite grains, the Ti# varied widely, from 16% ($\text{Fe}_{2.69}\text{Mg}_{0.19}\text{Al}_{0.07}\text{Cr}_{0.03}\text{Ti}_{0.1}\text{O}_4$, sample 727) up to 92.7% ($\text{Fe}_{2.75}\text{Ti}_{0.18}\text{Mg}_{0.04}\text{Al}_{0.3}\text{Ca}_{0.01}\text{O}_4$, sample 732).

We also observed a consistently high Mg# (number quantifying the amount of magnesium for Fe^{2+} substitution in the crystal structure, given by $100 \times [\text{Mg}/\{\text{Mg} + \text{Fe}^{2+}\}]$; see Fig. 5) of $\sim 70\%$ in most analyzed grains. Only sample 727 (point 1-6) showed a Cr# (number quantifying the ratio between chromium substitution with aluminum, where $100 \times [\text{Cr}/\{\text{Cr} + \text{Al}\}]$) of 30% (Table 1), indicating mafic to ultramafic contributions to the impact melt.

Sample 732 showed the widest range of composition. This sample was collected at the bottom of unit 3A, likely in the transition zone between the green schlieren and black melts (unit 3B).

In the impact melts of unit 3B, magnetic oxides are more abundant. They occur as small (10–50 μm) idiomorphic grains, larger than those in unit 3A, scattered within the melt's matrix, particularly in the uppermost samples (Fig. 4E). The chemical composition of unit 3B magnetite does not vary as much as in unit 3A, and it is generally consistent throughout the subunit (see representative samples 738 and 744, Table 1). Within the range of compositions observed in unit 3A, the grains in unit

Basement granitoid

Upper Impact Melt

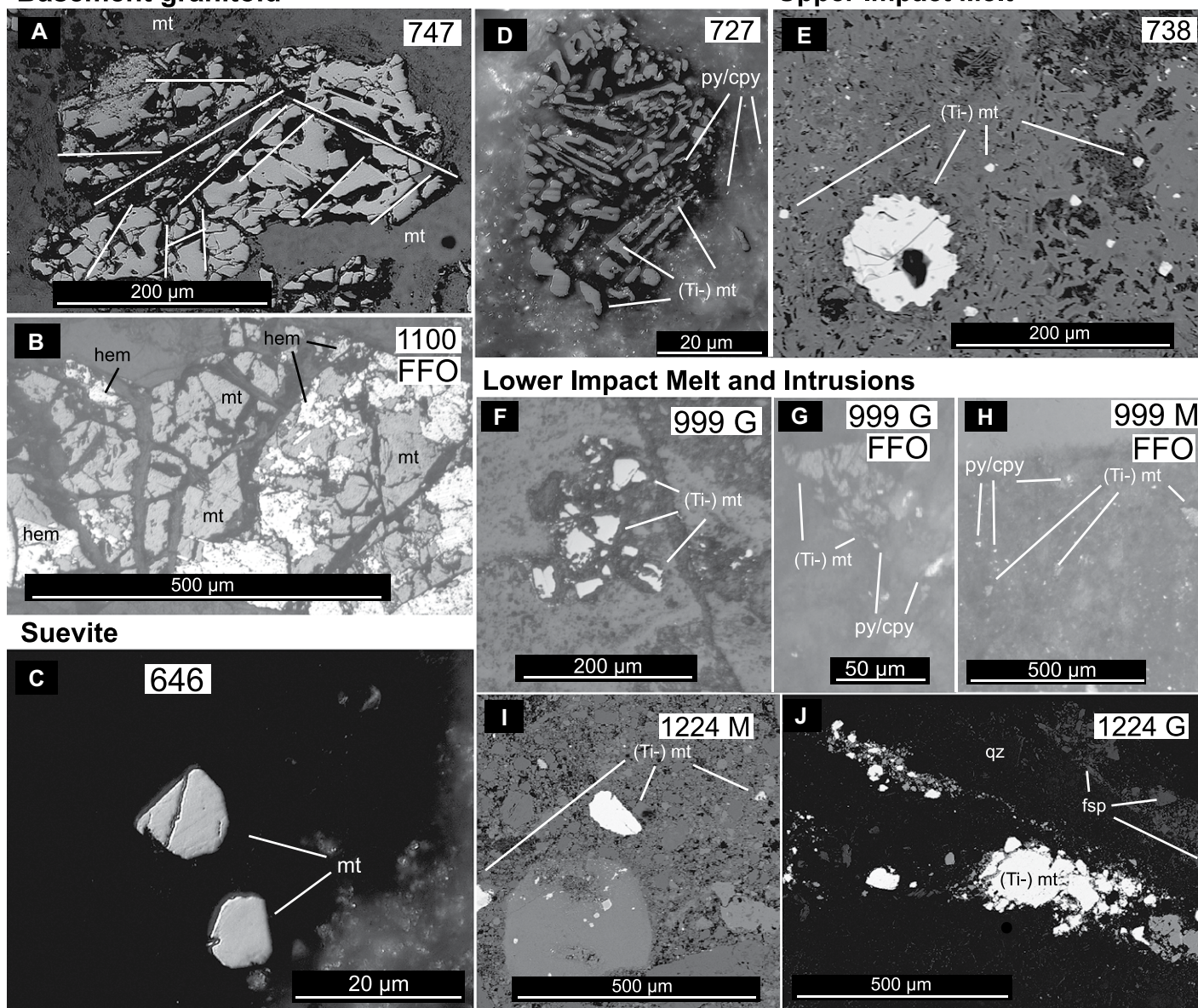


Figure 4. (A–D, F–H) Reflected light microscopy and (E, I, J) backscattered electron images of representative grains. Abbreviations: mt—magnetite, (Ti-)mt—titanomagnetite, hem—hematite, py—pyrite, cpy—chalcopyrite, qz—quartz, fsp—feldspar, M—melt, G—granitoid, FFO—ferrofluid. (A) Large (>200 μm) pure, fractured magnetite grain in the basement granitoid. Note shear fractures (white lines). (B) Very large (~1 mm) pure, fractured magnetite grain altered into hematite in the basement granitoid (polished section coated with ferrofluid). Note that shock fractures also occur in hematite, so both Fe-oxides predate the impact event. (C) Newly formed, small magnetite grains (~10 μm) in unit 2A. (D) Small skeletal grains surrounded by dusted sulfides in unit 3A. (E) Small grains of cation-substituted magnetite in the melt matrix of unit 3B, together with a larger grain of the same cation-substituted magnetite (in the center). (F) Fractured magnetite of sample 999 in contact with melt; note absence of hematite oxidation. (G) Fractured magnetite of sample 999 coated with ferrofluid. (H) Newly formed cation-substituted magnetite in sample 999 lower impact melt intrusion dike (unit 4) coated by ferrofluid. (I) Relatively large unfractured magnetite grains in melt of sample 1224. (J) Melt-injected, newly formed cation-substituted magnetite grains close to the contact of granite with melt (see Table 1 for mineral chemistry).

3B showed high-end concentrations of Al and Mg (Mg# ~60%) and Ti (up to TiO_2 ~5–7 wt% and Ti# up to 80%–85%). Magnetite formulas ranged from $\text{Fe}_{2.65}\text{Ti}_{0.19}\text{Mg}_{0.08}\text{Al}_{0.06}\text{Ca}_{0.01}\text{O}_4$ to $\text{Fe}_{2.67}\text{Ti}_{0.14}\text{Mg}_{0.10}\text{Al}_{0.07}\text{O}_4$.

In addition to chemical composition, Table 1 (and Supplemental Data S1) shows calculated Curie temperatures for single-point analysis in the magnetic minerals, using the empirical formula given in Engelmann (2008) based on

synthetic titanomagnetite (K was converted to $^{\circ}\text{C}$ after the calculation) and modified in Lied et al. (2020). The formula considers the cation substitution of Al and Mg, as well as of Cr and Mn, in samples that contain these elements. All

TABLE 2. HYSTERESIS PARAMETERS PRE- AND POSTHEATING TO 600 °C

Sample (unit)	Preheating		Postheating	
	Mrs/Ms	Bcr/Bc	Mrs/Ms	Bcr/Bc
727 (2A)	0.088	4.879	0.165	3.723
732 (3A)	0.036	6.665	0.089	2.762
738 (3B)	0.058	4.465	0.091	4.240
744 (3B)	0.051	7.406	0.081	3.325
747 (4)	0.060	4.435	0.063	3.913
804 (4)	0.093	3.327	0.107	3.543
995AG (4)	0.209	1.960	0.242	1.938
995AM (4)	0.172	2.170	0.207	2.000
999C (4)	0.232	2.111	0.258	2.014
1100 (4)	0.263	1.729	0.336	1.629
1100 (4)	0.244	1.763	0.303	1.688
1100 (4)	0.087	2.603	0.089	2.917
1194 (4)	0.051	3.658	0.053	4.249
1224C (4)	0.073	4.052	0.087	3.457
1224DG (4)	0.265	1.810	0.299	1.931

Notes: For details, see main text. Data are given in Supplemental Data S6 (see text footnote 1). Mrs—remanent magnetization; Ms—saturation magnetization; Bc—coercivity; Bcr—coercivity of remanence.

imity and association, with generally higher concentrations of Ti (Table 1). In sample 1224, some of the cation-substituted magnetite appeared along veins “injected” into the granite in contact with melt (Fig. 4J). In comparison to unit 3B, magnetite showed varying Ti concentrations (0.24–12.6 wt% TiO₂) with no Al and Mg substitution, and formulas ranging from nearly pure magnetite (Fe_{2.98}Ti_{0.01}O₄, 1224 III-9) to intermediate titanomagnetite (Fe_{2.62}Ti_{0.38}O₄, Ti# 100%, 1224 III-7). These compositions were found in the grains shown in Figure 4J, suggesting that there was poor element homogenization in the melts.

Magnetic Grain Size

Through hysteresis and background measurements we obtained the values for remanent magnetization (Mrs), saturation magnetization (Ms), coercivity (Bc), and coercivity of remanence (Bcr). We plotted these parameters on a Day diagram (Fig. 6A). The data shows that the ratios of the different lithologies plot along the multidomain (MD)–single domain (SD) mixing line for magnetite (Day et al., 1977; Dunlop, 2002; Lanci and Kent, 2003). The large, fractured basement magnetite showed predominantly pseudo–single domain (PSD) behavior, with five samples showing MD magnetite. Magnetite from suevite mostly showed PSD behavior. Melt samples from the upper impact melt tended to have higher Bcr/Bc ratios (>4), with the majority of the magnetite grains showing PSD + MD behavior. Large magnetic grain-size variation, with some clustering at the PSD–SD boundary (Bcr/Bc = ~2; Fig. 6A), was typical for magnetite from the lower impact melt.

For 20 samples, we measured hysteresis parameters before and after *k*-*T* measure-

ments in order to test the hypothesis that magnetic domain size changed due to annealing of lattice defects and mineral reactions. Six samples were rejected due to very weak/paramagnetic signals after heating. Upper impact melt samples showed a significant decrease of Bcr/Bc ratios and increase of Mrs/Ms ratios, from PSD + MD toward a more general PSD domain size behavior (Fig. 6B; Table 2), in line with the formation of new, smaller magnetite grains during heating. The lower impact melt and lower impact melt dikes manifested no change in Bcr/Bc but in general an increase of Mrs/Ms. Granitoid basement samples showed a small increase of the Bcr/Bc ratio, which was, however, not very significant. Two basement samples in contact with melts showed a decrease in Bcr/Bc ratios. Samples from the lower impact melt displayed a general increase of Mrs/Ms and no change in Bcr/Bc (Fig. 6B). Domain size changes in the cation-substituted magnetite after heating suggest a general pattern of grain-size reduction on the Day plot (Fig. 6B). Despite this, the interpretation of the Day diagram in cation-substituted magnetite is not without issues (see e.g., Roberts et al., 2018), and the mechanism through which this grain-size reduction occurred remains elusive.

The results of IRM component analysis are presented as normalized gradient acquisition plots (GAPs) in Figures 6C to 6F and in Tables S3 and S4 in the Supplemental Material. For the majority of the samples, a single-component distribution is favored, with mean coercivity (*B*_{1/2}) varying between 30 and 73 mT, which we identified as magnetite. For a few samples, we observed a high-coercivity component (*B*_{1/2} > 500 mT) with relatively low contribution (<14%), which we identified as hematite (see Figs. 6C and 6E). Sample 1100 showed two components before heating, with 95% and 5% contributions of magnetite and hematite, respectively, but only one low-coercivity component after heating (Fig. 6C; Table S4 in Supplemental Text). However, it should be noted that some components were skewed and did not fit to the log-normal distribution applied in the Excel workbook by Kruijver et al. (2001). As we could not include skewness in the component analysis, we decided not to use another low-coercivity component that would be artificial to fill the space below the left branch of the fitting line (see, e.g., Fig. 6F).

Hysteresis measurement data are given in Supplemental Data S6, and hysteresis parameters before and after heating experiments are given in Table 2. IRM component analysis data are in Supplemental Text, and raw data are in Supplemental Data S8.

Magnetic Transition Temperatures

Basement Granitoid

The basement granitoid samples from 747 to 1197 m were characterized by Verwey transitions between –157 °C and –151 °C in the first LT measurement (Table 3; Figs. 7A and 8). In a second LT measurement after a heating cycle, the Verwey transition showed a decrease in temperature up to 3 °C (Fig. 8). The transition was sharp, and Verwey peak ratios were around ~1.3, with a tendency to decrease to ~1.1–1.15 after the heating cycle (Fig. 8; Table 3). Curie temperatures of the granitoid samples ranged mostly from 572 °C to 585 °C (Figs. 7 and 8) and were largely the same in the heating and cooling curves. This observation indicates more or less stoichiometric magnetite, in agreement with the mineral chemical analysis (see Table 1). Hopkinson peak ratios were around 1.2–1.3, decreasing to 1.1–1.2 in the cooling curves (Fig. 8).

Most granitoid basement samples showed a positive *A*₄₀ below 50%, with magnetic susceptibility increasing after heating (Fig. 7A, sample 1100; Fig. 8). This behavior is often observed in rocks containing hematite, when *k*-*T* measurements are done in argon atmosphere (e.g., Just and Kontny, 2012). It implies the presence of a reducing agent in the argon gas (see Rock Magnetic Methods section), which enables the transformation of hematite (Fig. 4B) to magnetite. A notable exception is sample 747, which showed an essentially reversible behavior (*A*₄₀ of 3%). This was confirmed by our *M*-*T* results, where no sign of hematite was found during heating, and *T*_C is that of pure stoichiometric magnetite (Fig. 7E, sample 747).

Lower impact melt intrusions into the granitoid also showed magnetite with Curie temperatures around 570–580 °C, and these were not very different from the granitoid host rocks. However, they showed a negative *A*₄₀ (sample 847 and 1224 in Table 3; Fig. 7D), which seems to be characteristic for the impact melts and indicates an instability of the ferrimagnetic phase. A detailed description of a granitoid–lower impact melt contact is given in the section on “High-Resolution Profiles of the Lower Impact Melt–Granitoid Basement Contact” below.

Suevite

Suevites from units 2A and 2B (Fig. 7B) showed Verwey transitions between –165 °C and –150 °C and lower *T*_{VPR2} values after heating (*T*_{VPR2}; Table 3; Fig. 8). Suevites from unit 2A were characterized by a broad Curie temperature interval between ~500 °C to 580 °C and a suppressed, but faintly visible Verwey transition in the first LT measurement (Figs. 7B and 8). After heating to 700 °C, two better-defined Curie

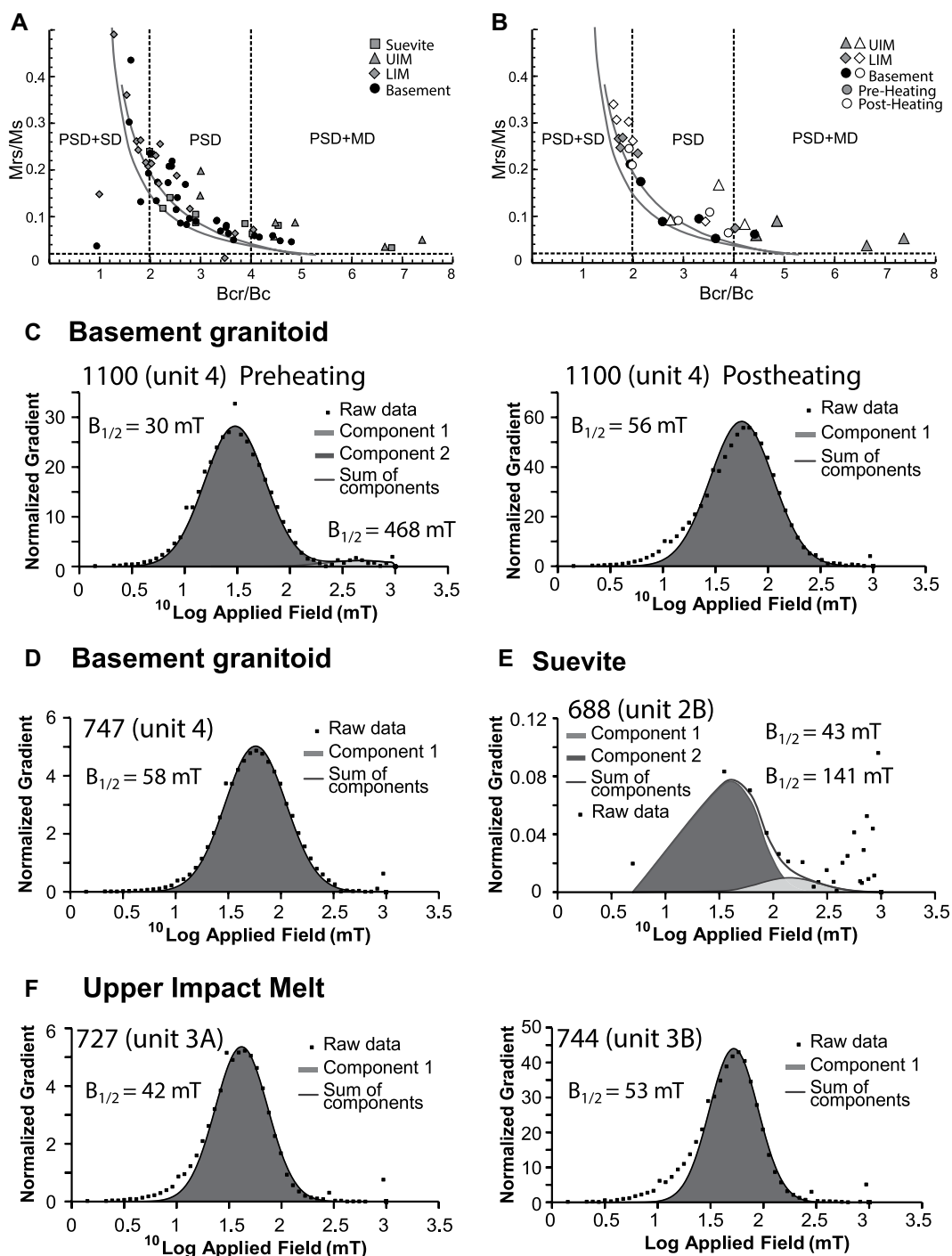


Figure 6. (A) Day-Dunlop plot (Day et al., 1977; Dunlop, 2002) for hysteresis data of our samples. Note preferential pseudo-single domain (PSD) behavior in the basement samples. (B) Day-Dunlop plot with pre- and postheating data of the 14 accepted samples. (C–F) Isothermal remanent magnetization (IRM) component analysis gradient acquisition plots (GAPs) for representative samples: (C) basement granitoid sample 1100 before (left) and after (right) heating (note the disappearance of the second, high-coercivity component after heating); (D) single-component solution for basement granitoid sample 747; (E) double-component solution for sample 688, which we identify as magnetite and hematite; and (F) upper impact melt representative samples from unit 3A (left) and 3B (right). M_r —remanent magnetization; M_s —saturation magnetization; B_c —coercivity; B_{cr} —coercivity of remanence; SD—single domain; MD—multidomain; UIM—upper impact melt; LIM—lower impact melt; $B_{1/2}$ —mean coercivity.

temperatures at 441 °C and 584 °C occurred in the cooling curve (Fig. 7B). Heating curves of suevites from unit 2B showed a small but sharp transition at 580 °C, and a prominent second transition in the cooling curve varying from 440 °C to 460 °C, with large HPRs (Table 3; Fig. 8). In the M - T curve for sample 646, a decrease of magnetization from 400 °C to 460 °C and a final Curie temperature at 570–580 °C were observed (Fig. 7E, sample 646).

These suevite samples showed the highest A_{40} alteration index (174%–345%), suggesting mineral transformation to a ferrimagnetic phase during heating (Table 3; Fig. 8). As the suevite contains high amounts of secondary carbonates (e.g., Kring et al., 2020), it is likely that they transform into Fe- and/or Mn-bearing spinel-group minerals (Just and Kontny, 2012). One of the ferrimagnetic minerals that is formed by these mineral reactions is stoichiometric magne-

rite, as evidenced by the Curie temperature close to 580 °C in the heating curve and the clear Verwey transition in the second LT measurement.

Upper Impact Melt

The uppermost samples of unit 3A did not show a Verwey transition, neither before nor after heating up to 700 °C (Fig. 7C). Samples between 732 and 744 mbsf did show a Verwey transition temperature but at significantly lower

TABLE 3. PARAMETERS DETERMINED FROM TEMPERATURE-DEPENDENT MAGNETIC SUSCEPTIBILITY (k - T) CURVES

Sample (unit)	T_{V1} (°C)	T_{V2} (°C)	T_{C1} (°C)	T_{C2} (°C)	T_{VPR1}	T_{VPR2}	HPR1	HPR2	A_{40} [40%]
639 (2A)	-151.00	-155.30	573.10	466.60	1.27	1.05	1.29	1.29	174.70
646 (2A)	ND	-155.00	491553	4411584	NA	0.95	1.28	1.34	207.66
683 (2B)	-150.00	ND	554.30	578.60	1.18	NA	1.34	2.45	411.44
688 (2B)	-158.90	-153.40	574.00	468.01581.1	1.23	1.01	1.02	2.29	345.48
700 (2B)	ND	-165.50	489.91592.2	442.61578.0	NA	1.01	1.34	1.23	-4.38
721 (3A)	ND	ND	537.80	481.11582.9	NA	NA	1.32	1.43	-26.25
727 (3A)	ND	ND	545.40	528.70	NA	NA	1.17	1.25	18.62
732 (3A)	-185.80	-186.30	521.10	481.10	1.13	1.02	1.01	1.12	-14.02
738 (3B)	-187.20	-188.60	512.70	438.20	1.08	0.98	1.08	1.22	-19.99
744 (3B)	-179.70	-184.20	511.80	472.50	1.08	0.97	1.24	1.21	-18.07
747 (4)	-153.40	-153.10	588.50	595.40	1.24	1.24	1.34	1.29	2.90
763 (4)	-157.70	-160.80	572.00	574.30	1.28	1.22	1.28	1.19	18.03
804 (4)	-154.10	-157.50	582.90	586.70	1.31	1.22	1.28	1.18	20.92
810 (4)	-159.80	-157.90	571.80	574.90	1.31	1.27	1.27	1.21	23.57
847 (4)	-159.10	-153.90	582.30	572.10	1.31	1.03	1.90	1.42	-23.87
967 (4)	-157.00	-157.50	572.40	578.00	1.29	1.22	1.23	1.12	15.87
982 (4)	-157.00	-156.30	574.30	578.60	1.31	1.18	1.17	1.10	37.84
994 (4)	-153.90	-155.30	551.80	577.40	1.30	1.19	1.17	1.15	26.25
995AM (4)	-156.50	-157.00	574.30	570.90	1.12	1.16	1.54	1.23	23.30
995AG (4)	-154.60	-156.00	575.50	579.90	1.24	1.07	1.12	1.21	7.36
995B (4)	-156.30	-156.70	572.40	573.70	1.32	1.24	1.28	1.17	48.86
996 (4)	ND	ND	552.80	566.90	NA	NA	1.48	1.19	89.20
997 (4)	-155.30	-155.10	573.70	576.10	0.97	1.19	1.73	1.26	16.67
999M1 (4)	-151.20	-163.40	579.20	579.20	1.19	1.09	1.34	1.26	-11.30
999M2 (4)	-156.00	-157.90	572.40	573.70	1.20	1.10	1.50	1.22	-14.25
999C (4)	-157.00	-154.30	570.60	575.80	0.98	1.05	1.45	1.82	-40.64
999G3 (4)	-152.70	-152.90	310.61570.3	581.10	1.26	1.54	1.31	1.73	-61.21
999G2 (4)	-152.40	-157.70	579.50	577.40	1.28	1.31	1.11	1.17	9.54
999G1 (4)	-152.40	-153.90	582.30	593.20	1.57	1.31	1.13	1.12	34.19
1085 (4)	ND	ND	572.40	570.60	NA	NA	2.25	1.63	197.57
1097 (4)	-153.10	-153.90	574.90	582.00	1.30	1.20	1.30	1.19	47.78
1100 (4)	-156.00	-159.10	572.80	576.50	1.33	1.24	1.28	1.19	45.00
1103 (4)	-155.50	-155.50	573.70	580.50	1.29	1.19	1.25	1.12	45.54
1135A (4)	-157.70	-159.80	575.80	580.50	1.32	1.23	1.20	1.12	19.32
1135B (4)	-146.90	-153.10	585.10	591.00	1.19	1.15	1.20	1.15	14.52
1137 (4)	-155.10	-157.00	581.10	577.10	1.30	1.27	1.28	1.10	166.36
1140 (4)	-159.10	-157.20	572.80	574.90	1.31	1.25	1.32	1.27	12.26
1149 (4)	-155.30	-156.70	573.70	578.30	1.28	1.17	1.18	1.26	49.64
1150 (4)	-155.80	-157.70	570.00	573.10	1.28	1.18	1.21	1.08	19.50
1161 (4)	-152.70	-158.60	577.40	582.60	1.30	1.26	1.26	1.19	16.86
1194 (4)	-155.80	-158.20	574.30	574.90	1.29	1.26	1.29	1.22	13.58
1197 (4)	-157.00	-156.70	570.30	576.10	1.33	1.24	1.12	1.10	14.52
1224A (4)	-157.00	-160.60	571.80	574.30	1.20	1.20	1.39	1.21	-1.24
1224B (4)	-162.00	-161.30	570.00	576.50	1.22	1.21	1.36	1.19	-2.21
1224C (4)	-160.30	-162.50	575.80	577.70	1.19	1.21	1.31	1.08	9.25
1224DG (4)	-160.30	-162.50	572.10	573.70	1.26	1.21	1.23	1.08	12.71
1224DM (4)	-164.10	-167.20	568.80	572.80	1.18	1.21	1.30	1.16	-18.71
1225 (4)	-164.80	-164.40	582.00	578.90	1.05	1.17	1.71	1.37	3.34
1231 (4)	-160.60	-164.60	571.80	577.10	1.21	1.21	1.23	1.16	8.84
1249 (4)	-167.40	-174.50	581.70	587.90	1.20	1.24	1.34	1.25	3.49
1326 (4)	-153.60	-164.40	579.90	584.50	1.17	1.16	1.27	1.15	58.80

Notes: Refer to Figure 3 for visual representation of these parameters and to the text for the formulas that were used. T_V —Verwey transition temperature (°C) before (T_{V1}) and after (T_{V2}) heating-cooling cycle; T_C —Curie temperature (°C) from heating (T_{C1}) and cooling (T_{C2}) curve; T_{VPR} —Verwey peak ratios for before (T_{VPR1}) and after (T_{VPR2}) heating-cooling cycle; HPR—Hopkinson peak ratios for heating (HPR1) and cooling (HPR2) curves; A_{40} [%]—alteration index A_{40} ; ND—no data; NA—not applicable.

temperatures (below -170 °C; see sample 744 in Fig. 7C) compared to stoichiometric magnetite (-153 °C) (Fig. 8). Heating curves showed distinctly higher Curie temperatures (512 – 545 °C) compared to those retrieved from the cooling curve (440 – 530 °C; Figs. 7 and 8; Table 3). The lower T_C in the cooling curves was also observed in the M - T curve (Fig. 7E, sample 727). The alteration index A_{40} was mostly negative and suggests a decrease of the ferrimagnetic phase during heating. All data for k - T measurements are in Supplemental Data S2; all M - T measurements are in Supplemental Data S3.

High-Resolution Profiles of Lower Impact Melt–Granitoid Basement Contact

To evaluate the thermal effect of the impact melt on the shocked magnetite from the granitoid basement rocks, we measured six k - T curves over an 8 cm profile across a basement granitoid–lower impact melt contact at 999 mbsf, investigated the magnetic phases microscopically, and performed IRM component analysis (Fig. 9). The k - T curves from the granitoid rock showed relatively good reversibility (G1 and G2 in Fig. 9). The A_{40} of G1 and G2 was 34% and 10%, respectively, which is lower than the aver-

age of the basement (around $\sim 45\%$). An alteration effect in form of a hump between 200 and 400 °C was observed only at a distance of < 1 cm from the contact (G3 in Fig. 9). This hump was particularly well exposed in the flow-foliated ultracataclasite (C in Fig. 9). IRM component analyses showed only one low-coercivity component with $B_{1/2} = 48$ – 51 mT in the granite samples and $B_{1/2} = 56$ – 62 mT in the melt samples.

The hump also faintly occurred in the impact melt (M1 and M2 in Fig. 9). While this hump disappeared in the cooling curves of the granitoid rock (G2, G3) and flow-foliated ultracatacla-

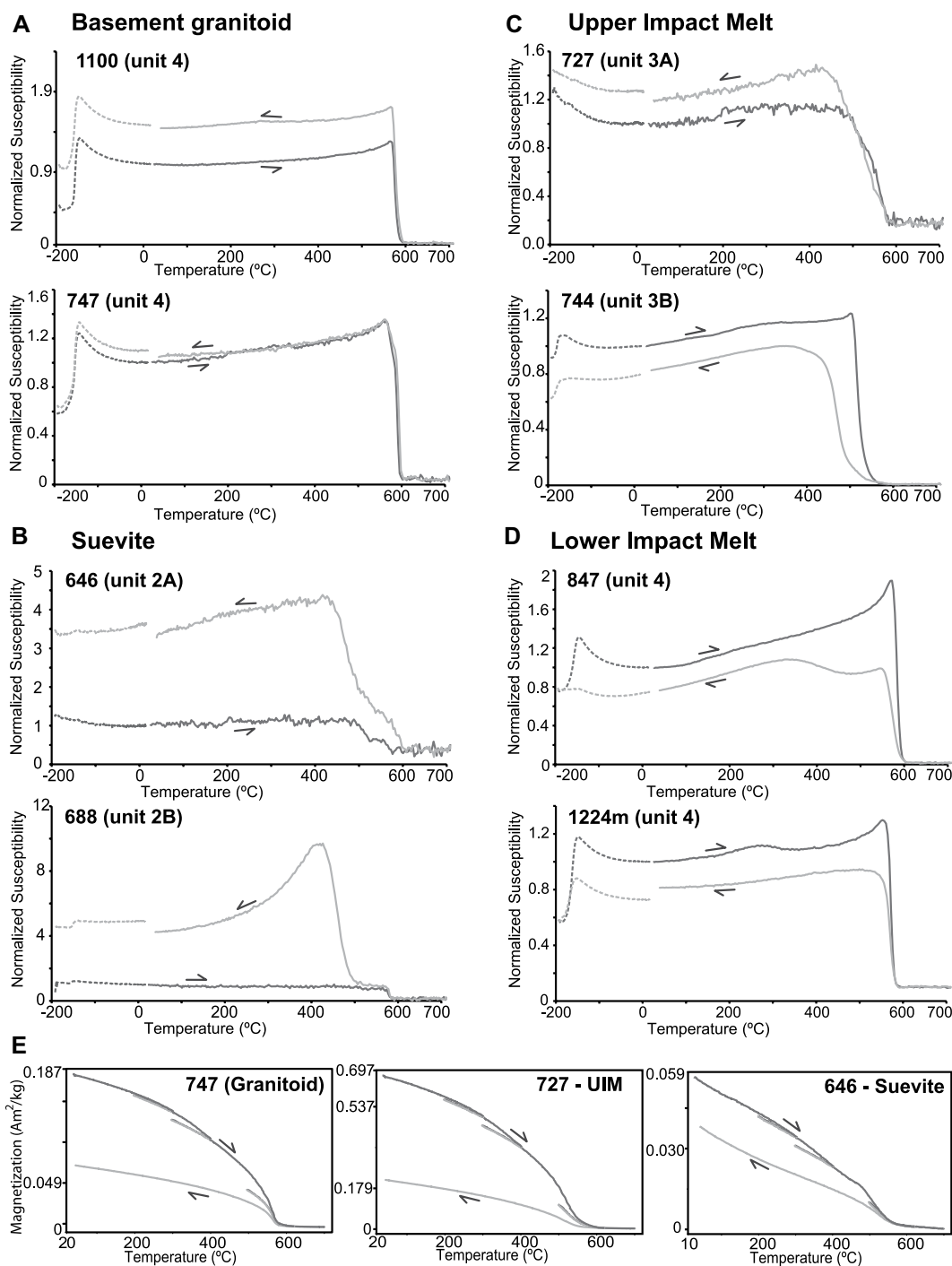


Figure 7. (A–D) Representative temperature-dependent magnetic susceptibility (k - T) curves from different lithological units of drill core M0077A: (A) granitoid basement; (B) suevite; (C) upper impact melt (UIM); and (D) lower impact melt. See main text for formulas and description of these parameters. Compare with Figure 8 for similarities of melt from sample 999. (E) Representative thermomagnetic (M - T) measurements for units 2, 3, and 4. All M - T curves were done in air atmosphere. Dark line is the heating curve, while lighter is the cooling curve. See Figure 3 for the description of the susceptibility parameters given in Table 3.

site sample (C), it remained visible in the impact melt samples (M1, M2), where it shifted toward slightly higher temperatures. Magnetite grains in the impact melt were too small for a reliable quantitative EPMA determination. However, the Curie temperature near 580 °C implies a close to stoichiometric composition of magnetite. The Hopkinson peak at the Curie temperature disappeared in the cooling run, suggesting that some annealing causes magnetic domain size growth

and/or a mineral reaction forming a non- or less-magnetic phase.

High-Temperature Annealing Experiments

To better understand the role of temperature in the postimpact processes that affected the magnetic mineralogy, we performed a stepwise heating/cooling experiment for sample 1100 from the granitoid basement (for susceptibility parameters, see Table 3) to investigate the onset of irreversible

behavior (Fig. 10A). Until 540 °C, the magnetic susceptibility of heating-cooling runs was reversible (Fig. 10A), but at 560 °C, we observed a significant irreversibility (20% increase in susceptibility) between the heating and cooling curves (Fig. 10B), with a decrease of the HPR from 1.38 to 1.24, suggesting a slight domain size increase (Dunlop, 2014; Kontny et al., 2018). The higher susceptibility and lower HPR were maintained in the next heating curve of the subsequent run

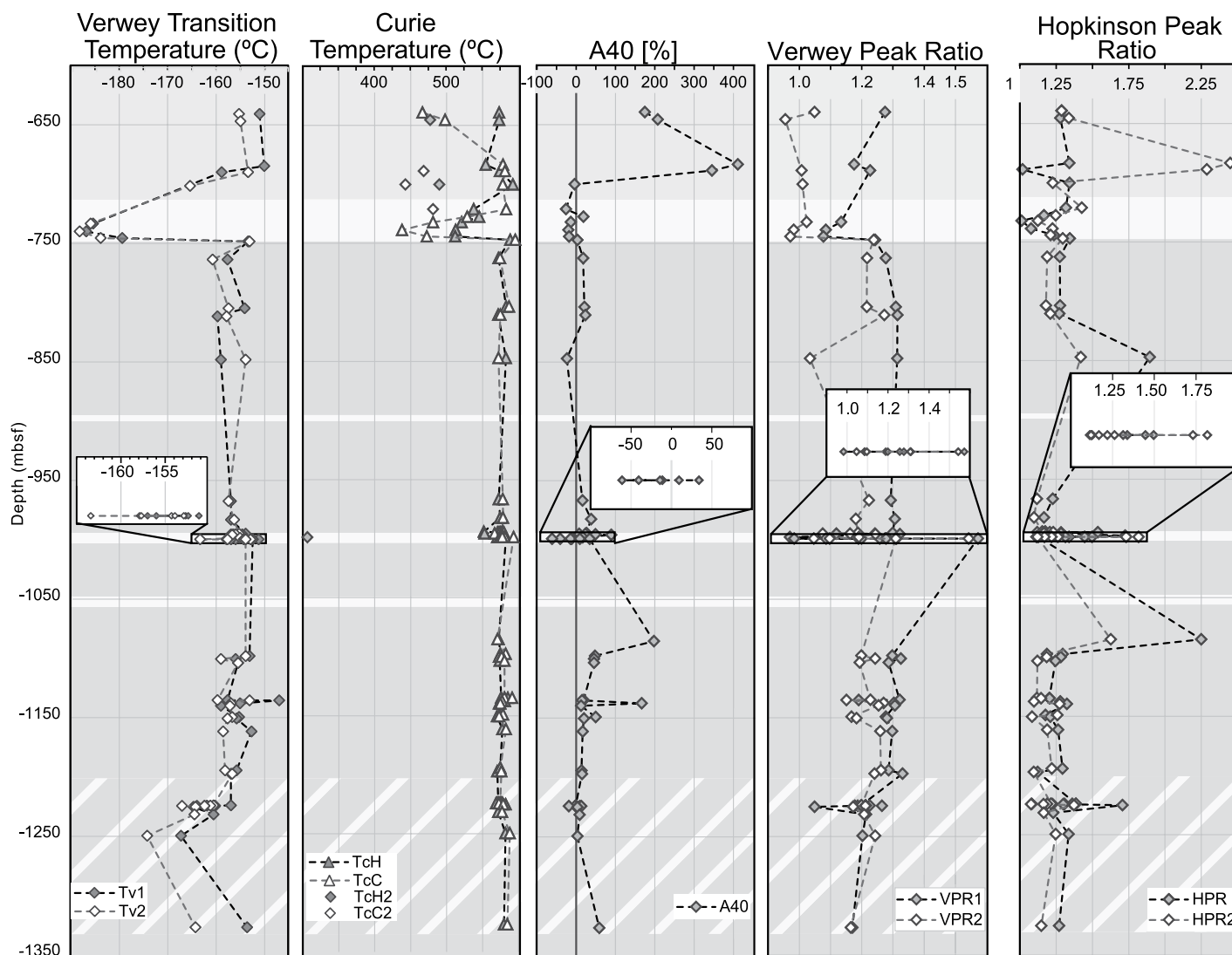


Figure 8. Depth variation of susceptibility parameters along core M0077A. Note: Verwey transition temperatures (T_V) are lower in the upper impact melt and lower impact melt units, while they remain relatively constant between $-151\text{ }^{\circ}\text{C}$ and $-159\text{ }^{\circ}\text{C}$ in the granitoid unit (unit 4). Curie temperatures (T_C) remain constant through unit 4, and both Verwey peak ratio (VPR) and Hopkinson peak ratio (HPR) show a decrease after the heating cycles, suggesting a magnetic domain size increase during the experiment. The background coloring is the same pattern as in Figure 2 (from top to bottom: suevite, upper impact melt, and basement granitoid [intercalated with lower impact melt dikes]). TcH—Curie temperatures (heating); TcC—Curie temperatures (cooling).

(to $580\text{ }^{\circ}\text{C}$) and showed once again a decrease in HPR from 1.29 to 1.27, however not as distinct as in the first experiment (Fig. 10B). In this curve, we observed also a slight increase of the magnetic susceptibility at the Hopkinson peak. This increase was smaller than the increase in the k - T curves observed elsewhere in the basement when regularly heated up to $700\text{ }^{\circ}\text{C}$, even in the same sample (sample 1100, see Fig. 7A). To quantify this change in magnetic susceptibility, we utilized the parameter A_{HP} (see calculation in “Methods”), which is related to the formation of new magnetite during heating. Sample 1100, when heated to $700\text{ }^{\circ}\text{C}$ (Fig. 7A), showed an A_{HP} value of 33.5%. In our annealing experiments, the

curve up to $560\text{ }^{\circ}\text{C}$ had an A_{HP} of 0.81%, while the curve up to $580\text{ }^{\circ}\text{C}$ had a value of 4.4%. This factor, combined with the positive A_{40} (14.9%) in the $580\text{ }^{\circ}\text{C}$ run, indicates that the formation of new magnetite initiated between $560\text{ }^{\circ}\text{C}$ and $580\text{ }^{\circ}\text{C}$. We attribute the original $\sim 20\%$ increase in susceptibility between $540\text{ }^{\circ}\text{C}$ and $560\text{ }^{\circ}\text{C}$ to domain size changes through annealing of the lattice defects.

To further investigate the hematite to magnetite transformation during heating in the shocked magnetite, we performed four repeated heating/cooling cycles from room temperature to a maximum of $700\text{ }^{\circ}\text{C}$ until we obtained full reversibility of the heating and cooling curve (Fig. 10C).

After the first cycle, the magnetic susceptibility increased by around 45% ($A_{40} = 45\%$) and showed a distinctly positive A_{HP} (26.5%). This irreversibility was related to a transformation of hematite intergrown with magnetite (as seen in Figs. 4B and 10D, preheating) to magnetite (Fig. 10D, postheating). This feature also agrees with an interpretation that positive A_{40} values ($<50\%$ in our basement samples) and well-defined magnetite Curie temperatures at $\sim 580\text{ }^{\circ}\text{C}$ are indicators for a hematite to magnetite transformation when measured in an argon atmosphere, as already suggested by Just and Kontny (2012). In addition, we observed a decrease in the HPR from 1.35 to 1.17, indicat-

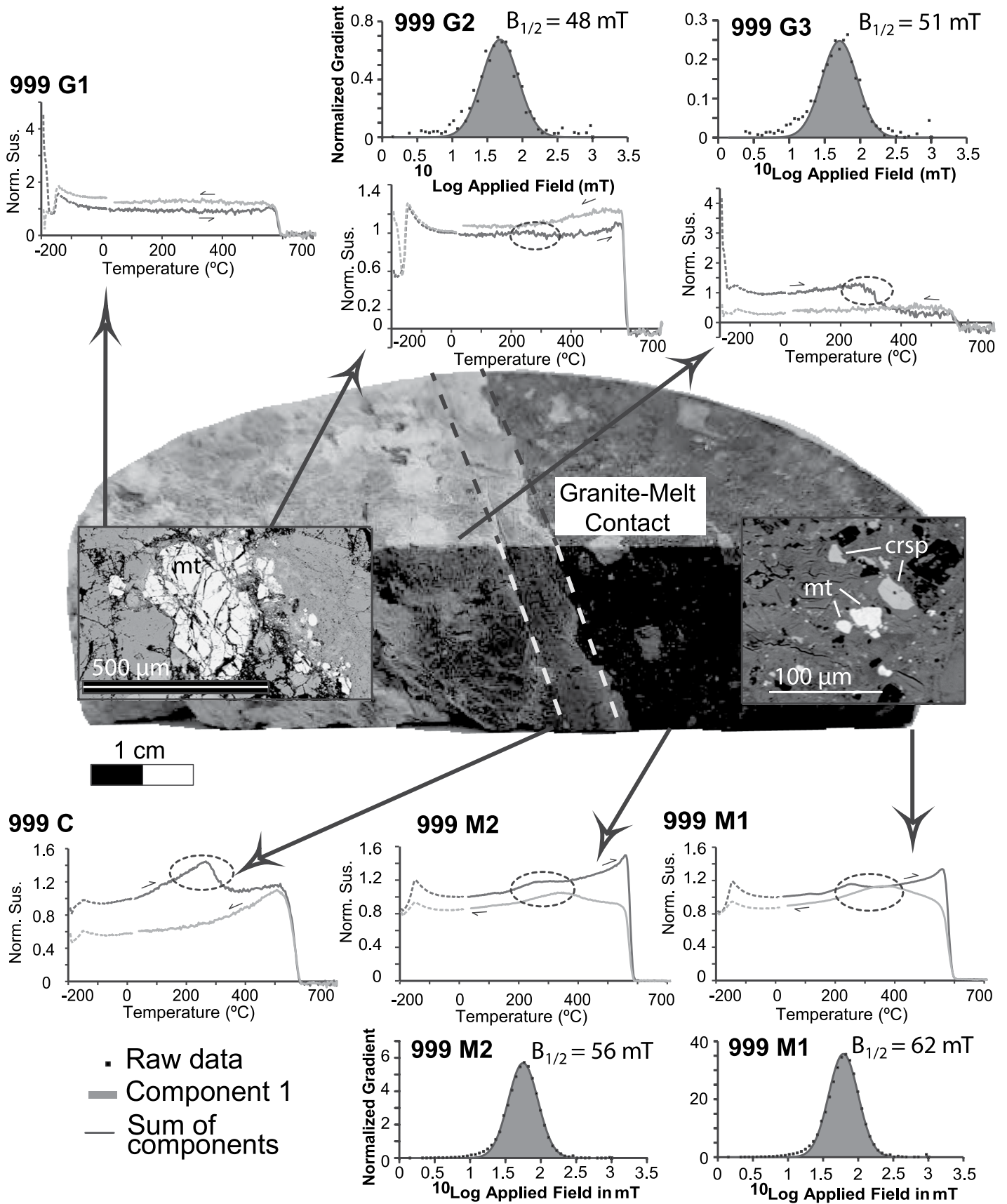


Figure 9. High-resolution temperature-dependent magnetic susceptibility (k - T) curves and isothermal remanent magnetization (IRM) analysis at the granitoid rock–ultracataclasite–impact melt contact of sample 999. Note the increased prominence of a hump in the heating curve toward the contact and in the melt region. Note also the texture differences between the large, fractured magnetite in the granite (left) and the small grains of newly formed magnetite in the melt (right). Norm. Susc.—normalized susceptibility; mt—magnetite; $B_{1/2}$ —mean coercivity; crsp—chromian spinel.

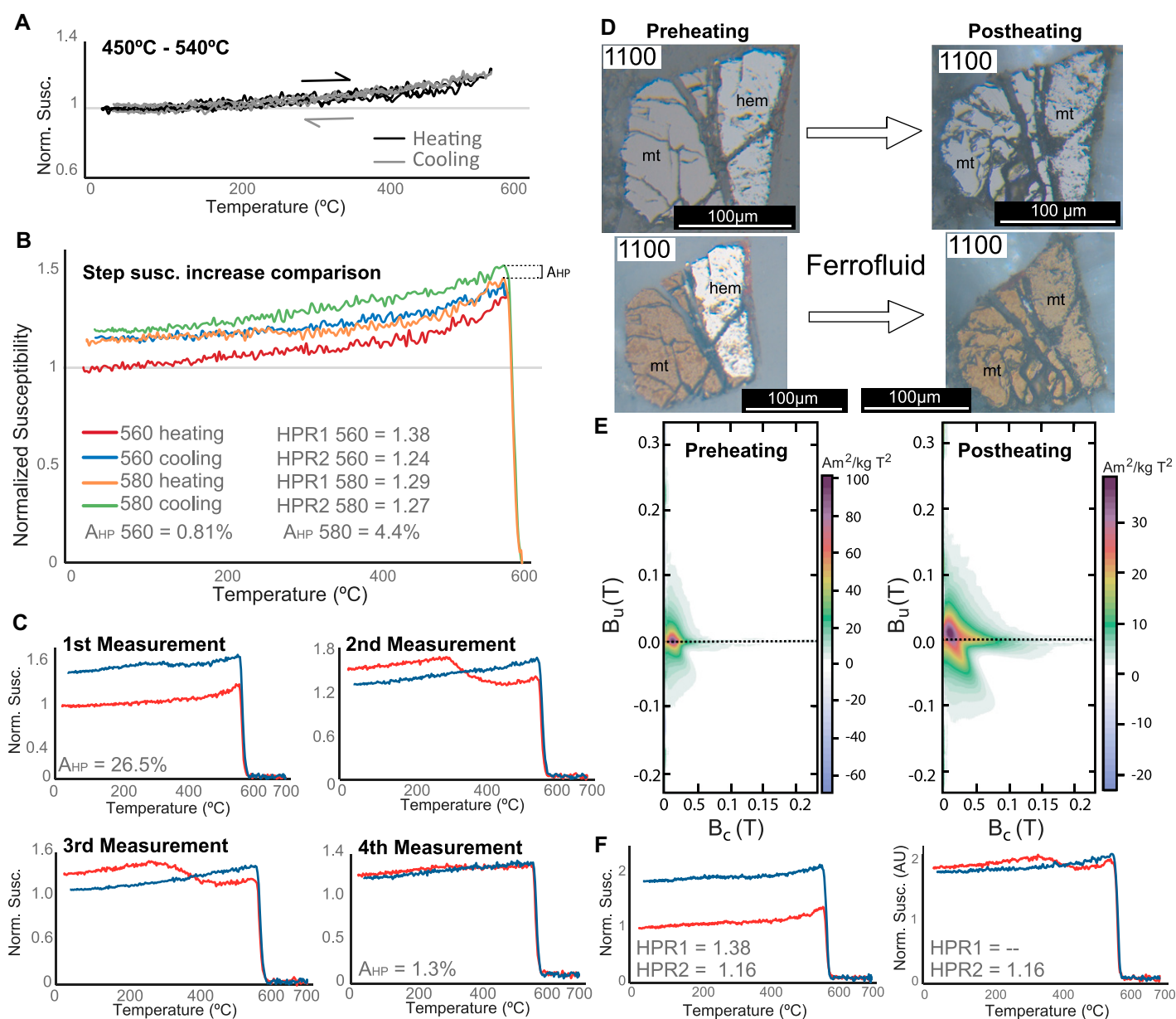


Figure 10. Stepwise heating/cooling experiments in argon atmosphere for sample 1100. (A) Consecutive heating steps to 450 °C, 500 °C, 520 °C, and 540 °C show reversible behavior. (B) At 560 °C and 580 °C, irreversible behavior occurs. Hopkinson peak ratio 1 (HPR1) was determined from the heating curve, and Hopkinson peak ratio 2 (HPR2) was determined from the cooling curve (details in text). Susceptibility was normalized to room temperature value of the 560 °C heating curve (red). (C) Four consecutive measurements up to 700 °C until reversibility is reached (heating in red, cooling in blue). Susceptibility was normalized to the room temperature susceptibility of the first measurement. (D) Magnetite and hematite of sample 1100 before (left) and after (right) first heating experiment up to 700 °C. Note the incomplete oxidation of the magnetite along the grain boundaries. After the heating experiment, hematite is completely transformed into magnetite. (E) First-order reversal curve (FORC) diagrams before (left) and after (right) the same heating treatment as described in D. (F) Repeated experiments with different heating/cooling rates (slow on the left, fast on the right). See text for details. Norm. Susc.—normalized susceptibility; mt—magnetite; hem—hematite; B_c —coercivity; B_u —interaction field.

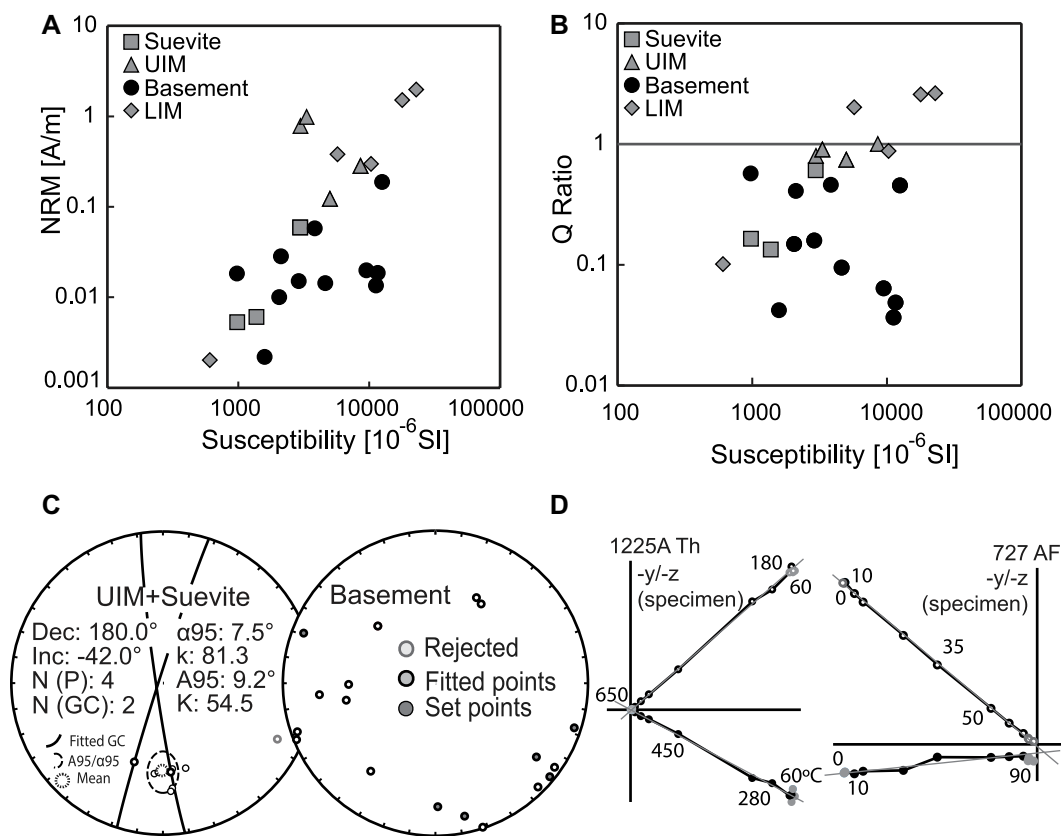


Figure 11. (A) Natural remanent magnetization (NRM) vs. magnetic susceptibility for selective samples. (B) Q ratio ($=\text{NRM}/kB$) vs. magnetic susceptibility. (C) Paleomagnetic results for impactites (suevite and impact melt, left) and granitoid basement (right). (D) Representative Zijderveld diagrams and interpretation of paleomagnetic directions for thermal (“Th,” left) and alternating field (AF) demagnetization (right). UIM—upper impact melt; LIM—lower impact melt; Dec—declination; Inc—inclination; P—set points; GC—great circles.

ing annealing of the defects in the shocked magnetite (e.g., Kontny et al., 2018).

The FORC of sample 1100 preheating (Fig. 10E, left) showed a PSD (vortex) behavior with some indication of interactions between particles and coercivities up to 50–60 mT. After heating (Fig. 10E, right), the sample still showed a well-defined PSD behavior, with a higher coercivity tail up to 150 mT. While still PSD, this may suggest the presence of newly formed SD particles during heating. After heating, we also observed an upward shift of the FORC and more asymmetric contours, which may signal an increase in interactions between magnetic particles (e.g., Roberts et al., 2014).

IRM component analysis also showed a significant increase in coercivity in the measured grains from this sample after heating. Original $B_{1/2}$ values in 1100 ranged from 30 mT to 63 mT preheating, while postheating, there was a systematic increase of coercivities in all samples, ranging from 53 to 72 mT. All samples showed an increase in coercivity, which may suggest an increased contribution of SD magnetite in the samples after heating (see Table S4).

Subsequent second and third cycles showed a hump in the heating curve, which can suggest either a transformation between 300 °C and 400 °C into a phase with lower magnetic suscep-

tibility compared to magnetite (likely maghemite or hematite) or a thermal relaxation effect of superparamagnetic magnetite. As we did not observe oxidation during our measurements in an argon atmosphere (see, e.g., Fig. 10D, postheating), this irreversibility is more likely a grain-size effect of superparamagnetic to SD magnetite grains (e.g., Zhao and Liu, 2010; Gao et al., 2019) during the transformation from hematite to magnetite. After the fourth heating cycle, heating and cooling curves were reversible and reached a state where magnetite was the only stable phase (A_{HP} of 1.3%). This behavior is similar to that of granitoid sample 747, which occurred close to the basement–upper impact melt contact (A_{HP} of 0.81%) (Fig. 7A). When a slower cooling rate (7 °C/min) was used (Fig. 10F), the shape of the first curve was the same, while a second cycle (using again the standard heating/cooling rate of 12 °C/min) showed a nearly reversible curve, suggesting the transformation is not only temperature dependent, but also time-of-exposure dependent.

Rock Magnetic and Paleomagnetic Data

Rock Magnetic Properties

The Koenigsberger ratio (Q ratio), given by $Q = \text{NRM}/(kB)$, where B is today’s magnetic

field, and kB is induced magnetization, gives the relative importance of remanent ($Q > 1$) or induced magnetization ($Q < 1$) for a given lithology (measurement data are provided in Supplemental Data S5). The NRM and susceptibility values of the basement and suevite samples were both quite low, with a dominance of induced magnetization ($Q < 1$; Figs. 11A and 11B). The upper impact melt and lower impact melt units showed both higher NRM and susceptibility values (Fig. 11A), and a similar contribution of induced and remanent magnetization ($Q \approx 1$; Fig. 11B). In general, our data showed a positive correlation ($R = 0.83$) between NRM and magnetic susceptibility in the impact lithologies, suggesting that the amount of magnetite controls the NRM. This is not the case in the basement granitoid, with a more scattered distribution ($R = 0.48$).

Paleomagnetic Directions

AF (7 samples) and thermal (16 samples) demagnetization showed two distinct groups of magnetic directions between the basement and the impactite samples (Figs. 11C and 11D). After the azimuth corrections based on drill core rotation were applied, we were able to interpret both declination (Dec) and inclination (Inc) of our paleomagnetic results. The granitoid base-

ment samples ($n = 17$) showed scattered directions, without a discernible pattern. On the other hand, the impact melt samples ($n = 4$) showed a clear clustering around Dec/Inc: $\sim 180^\circ/-40^\circ$ (Figs. 11C and 11D). In the suevite samples of unit 2A ($n = 2$), we fitted and anchored two samples as great circle interpreted points following the approach described in McFadden and McElhinny (1988), combining great circles and linear best fits. The remaining suevite sample 683 (unit 2B) was the only direction excluded by a 45° cutoff around the average directions. This, together with the anchored great circle fits for unit 2A, demonstrated both the uncertainty and the variability of paleomagnetic directions in unit 2. Data files are given in Supplemental Data S7 (in Paleomagnetism.org 2.0 format; Koymans et al., 2020).

DISCUSSION

Mineral Magnetic Characteristics

In the lithological units from the Chicxulub peak ring drilled at site M0077A, we distinguished three types of magnetite related to different impact-induced processes: pure, shocked magnetite in the granitoid basement, cation-substituted magnetite crystallized from the impact melt, and pure magnetite formed from hydrothermal fluids, although the latter played a subordinate role. These magnetite types were essentially the only magnetization component in our M0077A samples.

The pure magnetite in the basement granitoid belongs to the pre-impact Carboniferous magmatic mineral assemblage and is the original carrier of magnetization. This magnetite shows local pre-impact transformation to hematite (Figs. 4B and 6C, preheating); it was heavily fractured by the impact, and its hysteresis parameters show a wide variation (Fig. 6A), suggesting domain size changes from a likely original MD state. The Curie temperature at $\sim 578^\circ\text{C}$ and the Verwey transition, usually between -151°C and -163°C , suggest that this magnetite is close to stoichiometric. The slight shift of the Verwey transition toward lower temperatures (Fig. 8) compared to pure magnetite (-153°C ; Verwey, 1939) either indicates a certain amount of non-stoichiometry in $\text{Fe}_{3(1-\delta)}\text{O}_4$, or cation substitution (e.g., Özdemir and Dunlop, 1997). Microprobe analysis (Table 1) and a sharp Curie temperature at 580°C indicate that magnetite grains from the basement granitoid are rather slightly oxidized than cation-substituted. From the lower T_V values, we estimated that vacancies (δ) in magnetite are very low, $\sim 0.001 < \delta < 0.00125$ (Aragón et al., 1985). Slight oxidation is omnipresent in magnetite in all geologic settings (e.g., Vahle

et al., 2007; Zhang et al., 2020, 2021). In the case of Chicxulub, it is likely concentrated along shock-induced fractures and grain boundaries in magnetite and appears to be a common feature in shocked crystalline basement rocks (e.g., Mang and Kontny, 2013; Kontny and Grothaus, 2017). For the Chesapeake Bay impact structure, Mid-Atlantic coast of the United States, Mang and Kontny (2013) suggested that both fractured magnetite from the basement and very small, newly formed magnetite grains in the suevite are very sensitive to surface oxidation. Therefore, oxidation of magnetite may preclude its use as a reliable pressure indicator for impact structures, if the Verwey transition is considered (Carporzen and Gilder, 2010; Reznik et al., 2016).

The k - T curves from the Chicxulub basement show mostly irreversible behavior (see sample 1100 in Fig. 7A and Supplemental Data S2) if measured in an argon atmosphere. This behavior is typical for the occurrence of magnetite and hematite, where the latter is transformed to magnetite above a temperature of $\sim 580^\circ\text{C}$ (Figs. 4B and 10D). This mineral reaction is probably an artifact of the inert argon gas, as even in high purity, it can contain traces of hydrocarbon gases like CH_4 . However, this effect helps to identify Fe-bearing minerals due to their typical mineral reactions (e.g., Just and Kontny, 2012). Reversible behavior indicative of magnetite-only compositions occurs at the top of unit 4 near the boundary to the upper impact melt (Figs. 4A and 7A, sample 747) and in the vicinity of intercalated melt rock layers within the lower impact melt (Figs. 8 and 9, G2) and is interpreted as a high-temperature overprint due to the proximity to the impact melt. IRM analyses confirm the absence of hematite (e.g., Figs. 6D and 9, granitoids) in these samples.

Low A_{40} values indicate a nearly reversible behavior, while distinctly positive values (commonly $< 50\%$ in the basement granitoids; see Table 3; Fig. 8) indicate the hematite transformation into magnetite during heating in an argon atmosphere (Table 3; Fig. 8; see also Just and Kontny, 2012). If only pure magnetite occurs in the samples, it can be assumed that there was no alteration to hematite before the impact, or that hematite has been transformed back to magnetite in the presence of high enough temperatures ($> 580^\circ\text{C}$) during or after the impact event, as our heating experiment shown in Figure 10B suggests. Sufficiently elevated temperatures for this reaction were likely reached in the proximity of impact melts, for which temperatures between $\sim 650^\circ\text{C}$ and 750°C in the upper impact melt are reported (de Graaff et al., 2022).

In the basement, the large range of hysteresis properties across the PSD field (Fig. 6A) is noteworthy, as magnetite grains with $> 100\ \mu\text{m}$ are

expected to be in the MD field. This discrepancy can be attributed to two factors: (1) the fracturing of large grains into smaller individual grains, and (2) the formation of crystal lattice defects inside the larger grains (Reznik et al., 2016). The lattice defects will cause the domain walls to become pinned (e.g., Lindquist et al., 2015) and effectively reduce domain size in an otherwise MD grain. This mechanism is confirmed by the reduction of the Hopkinson peak ratios after heating, which occurs as a result of thermal annealing. Transmission electron microscopy on an experimentally shocked magnetite has shown that shock-induced defects in magnetite can recover after thermal treatment through recrystallization of magnetite and nucleation of new magnetite nanograins along microfractures (Kontny et al., 2018). These mechanisms, combined with thermally induced relaxation of slightly distorted lattices in the unfractured sections of the magnetite, may cause “unpinning” of the domain walls, and thus apparent domain-size growth during the heat treatment (Kontny et al., 2018). However, hysteresis data before and after heating in an argon atmosphere to 600°C revealed only slight changes for magnetite from the granitoid basement (Table 2; Figs. 6B and 6C), suggesting that fracturing is the more important mechanism in the Chicxulub basement. However, it has to be mentioned that the hysteresis data after heating do mask the annealing of lattice defects due to the formation of small magnetite grains from hematite, and therefore their contribution might be underestimated.

Cation-substituted (Ti, Mg, and Al) magnetite is present in both impact melt units, and it was even injected into the granitoid basement, where it occurs as small, skeletal grains (e.g., Fig. 4J). These grains are not fractured and show no signs of shock deformation, but they do have a large range of compositions (Table 1; Fig. 5; Supplemental Data S1). Both upper and lower impact melt units show similar compositions, denoting a granitoid and dolerite mixed-melt source; however, different quenching histories are reported (de Graaff et al., 2022). Unit 3A likely cooled at the fastest rates, especially in its upper portions, where water re-entry into the crater would have caused very fast quenching. Here, the newly formed cation-substituted magnetite is enriched in Mg and Al; whereas in the lower upper impact melt (unit 3B) and lower impact melt, Ti substitution dominates. As for both impact units, the whole-rock major elements are similar (de Graaff et al., 2022), but the source of the Mg- and Al-substituted magnetite may have been different. Ebel and Grossman (2005) reported unaltered grains of magnesioferrite spinel from spherules occurring at the Cretaceous-Tertiary stratigraphic boundary worldwide and suggested

from thermodynamic modeling that this phase formed due to sequential condensation of solids from the plume of vaporized carbonate and anhydrite target rocks. Therefore, the Mg- and Al-substituted magnetite grains may be a result of some admixing of carbonate melts in the uppermost upper impact melt unit.

The green schlieren in unit 2C and unit 3A show Mg-dominated magnetite compositions ($\text{Fe}_{2.69}\text{Mg}_{0.19}\text{Al}_{0.07}\text{Cr}_{0.03}\text{Ti}_{0.01}\text{O}_4$), with higher Curie temperatures (T_C) in the heating curve than in the cooling curve, and no Verwey transition (T_V ; Fig. 7; Table 3). The irreversibility of T_C in the heating and cooling curves can be expressed by ΔT_C ($\Delta T_C = T_{C\text{-Heating}} - T_{C\text{-Cooling}}$) and varies between 17 °C and 106 °C. Such an irreversibility can be either explained by cation ordering processes during the heating and cooling experiments (e.g., Harrison and Putnis, 1998, 1999; Lattard et al., 2006; Bowles et al., 2013), by vacancy-enhanced nanoscale chemical clustering in the octahedral sublattice (Bowles et al., 2019), or by maghemitization (e.g., Bowles et al., 2019; Lied et al., 2020; Zhang et al., 2021). At magmatic temperatures, the cation distribution in the inverse spinel structure is highly disordered, and the closure temperature defines the temperature at which reordering rates become so slow that a cation ordering state is frozen (Jackson and Bowles, 2014).

Positive ΔT_C values have been reported for pyroclastic deposits by Lied et al. (2020), Bowles et al. (2013), and Dudzisz et al. (2022). They occur in cation-substituted magnetite that is quenched very rapidly from magmatic temperatures through the closure temperature. If the temperature after deposition remains constant for a certain time interval, then the cation distribution evolves toward equilibrium for this specific temperature, increasing the degree of order and T_C (Jackson and Bowles, 2014). Therefore, T_C in cation-substituted magnetite with an inverse spinel structure depends on the degree of ordering, and it is lower for a fully disordered arrangement compared to a perfectly ordered one (Harrison and Putnis, 1999). The effect of different cation substitutions in natural cation-substituted magnetite has not yet been investigated in detail, but studies from Bowles et al. (2013, 2018, 2019) and Lied et al. (2020) point to significant differences in ΔT_C , especially if Mg and Al are involved.

Interestingly, in samples with lower cation substitution but with a higher Mg concentration (compare samples 721 with 738 in Tables 1 and 3), T_V is suppressed, suggesting that Mg substitution has a stronger suppressing effect on T_V than Ti substitution. Below T_V , the relatively free electron hopping between Fe^{2+} and Fe^{3+} in the octahedral site halts, leading to a sharp increase

in resistivity (up to three orders of magnitude; e.g., Bialo et al., 2019). Since Mg occupies the position of Fe^{2+} in the octahedral sites of the inverse spinel structure (see, e.g., Bowles et al., 2019, and references therein), an increase in Mg leads to a reduction of the total amount of Fe^{2+} , and this increases the $\text{Fe}^{3+}/\text{Fe}^{2+}$ ratio. An increase of this ratio has been associated with an increase in resistivity at $T > T_V$ (e.g., Mi et al., 2009), leading to a lower resistivity difference below and above T_V , and thus suppressing the intensity of the transition.

The cation-substituted magnetite from the impact melt acquired a thermal remanent magnetization (TRM) with the expected directions for chron 29r at the time of the impact (Dec/Inc = 180°/−40°; Fig. 11C), which agrees with earlier studies (Gulick et al., 2019). These are the only samples in our study with a Q ratio close to or above 1, which indicates the magnetization is dominated mostly by the remanent magnetization, suggesting these directions are the only reliable paleomagnetic directions in our study.

A third type of magnetite is represented by very small (<5 μm) unshocked and unfractured grains (Table 1; Fig. 4E). These grains were found throughout the core in all lithological units, particularly in regions with strong hydrothermal alteration, or in fractures of the basement, and often in assemblages with sulfides such as pyrite or chalcopyrite, and sometimes hematite. This magnetite did not constitute a main magnetic carrier in any of our samples, with the potential exception of the topmost two samples from unit 2A suevites, where we measured sections without basement clasts. We consider this magnetite to be secondary and associated with hydrothermal percolation. Because its abundance is low, it is the least important magnetite type, as its contribution to the samples' magnetic properties is subordinate.

Effect of the Postimpact Hydrothermal System on Shocked Magnetite

Despite the fact that hydrothermally formed magnetite may only be of magnetic significance in some sections of the upper suevite layers, postimpact hydrothermal alteration is prevalent throughout the whole peak ring. Higher-temperature (>250 °C) secondary minerals tended to form in the shocked crystalline basement, while low-temperature (<250 °C) hydrothermal minerals are concentrated in the upper 130 m of impactive lithologies (Kring et al., 2020), where vertical alteration channels are interpreted as indicators of postimpact hydrothermal venting. Paleomagnetic data have been interpreted by some authors to suggest a long-lived hydrothermal system that extended from the reverse chron

29r to a younger, normal polarity interval (Kring et al., 2020). On the other hand, other authors have argued that the large scattering of positive and negative inclinations suggests instead these layers retained their primary magnetization post-depositional NRM (i.e., temperatures were not high enough to induce remagnetization; Gulick et al., 2019). These interpretations may be reconciled, as inhomogeneity in the suevite units may lead to some regions having their NRM carried by newly formed hydrothermal magnetite or local chemical remanent magnetization acquisition (which can be imparted at any temperature, and could potentially have chron 29r and younger directions; see great circle interpretations in Fig. 11C). Other sections may be dominated by basement clast magnetite that maintained primary NRM directions (likely scattered during the cratering process) in the absence of high enough temperatures to “reset” the NRM vector (see rejected gray dot in Fig. 11C, Suevite + upper impact melt panel). We are hesitant, however, in making definitive claims regarding these directions, as we consider our paleomagnetic data obtained from unit 2 to be unreliable (Q ratios $\ll 1$; Fig. 11A). The basement magnetite was also not remagnetized by the hydrothermal system, as remagnetization would have homogenized the NRM directions. This is not the case, as we observed scattered “Basement” directions (Fig. 11C, Basement panel; Supplemental Text and Supplemental Data S7).

After the impact, the cooling of the large impact melt pool in the central basin of the crater created a long-lived hydrothermal system (up to 2 m.y.; Kring et al., 2020), with neutral pH conditions and starting temperatures of 350–450 °C. The fluids are expected to have evolved into a more reducing composition with time, but temperatures would have remained relatively high (Kring et al., 2020). These are the fluids that formed the hydrothermal magnetite observed in our investigated samples.

In close proximity between melt and basement (e.g., samples 995, 999, and 1224D; Fig. 8), we observed a hump between 200 and 400 °C in k - T curves that either indicates metastable maghemite (Zhang et al., 2020, 2021) or thermal relaxation due to nanometer-sized magnetite particles of different diameter (Zhao and Liu, 2010). In natural samples, we encounter this hump in regions of higher porosity, such as the ultracataclasite at the boundary between the melt and the granitoid, and in the 130-m-thick suevite and impact melt layer. These are samples where we would expect hematite to magnetite transformation due to the reducing fluids accompanied by the formation of new, small magnetite grains with a mottled texture, simi-

lar to what we observed in our transformation experiments during heating (Figs. 10B and 10C). While bulk-rock hysteresis results are inconclusive regarding thermal annealing (Fig. 6B), our IRM component analysis and FORC diagrams show a consistent increase in coercivities after thermal annealing in the granitoid (Figs. 6C and 10E). We suggest that this increase in coercivity is due to magnetic exchange coupling interaction between newly formed SD magnetite particles formed during the transformation of hematite to magnetite.

In the granitoid basement, postimpact hydrothermal alteration of magnetite is not that severe (alteration index A_{40} ranging from 3% to 90%) as in the impact rock units 2 and 3. Only locally, a stronger alteration of magnetite is indicated by $A_{40} > 100\%$ (Table 3), or in the proximity of the lower impact melt dikes (see sample 999 G3; Fig. 9; Table 3). Magnetite transformation into hematite (martitization) is a widespread phenomenon in crustal rocks (e.g., Lagoeiro, 1998), and it is a general phenomenon in hydrothermally altered magnetite-bearing granites. The alteration index can be used to detect hydrothermally induced oxidation of magnetite into hematite, as previously mentioned (see section “High-Temperature Annealing Experiments”; also, e.g., Just et al., 2004; Just and Kontny, 2012). Feignon et al. (2021) described a hydrothermal metasomatic event that occurred in the Permian ~50 m.y. after the Variscan emplacement of the granite in the Maya block, which likely caused this martitization before the impact.

Ishihara (1979) and Ishihara et al. (2000) investigated the magnetic susceptibility of Mesozoic and Cenozoic batholiths of Japan and Peru and suggested a value of 3×10^{-3} SI (300×10^{-5} SI units) units as the boundary dividing magnetite- and ilmenite-series granitoids. In the shocked granitoid basement of the Chicxulub peak ring, magnetic susceptibility values range between 50×10^{-5} and 300×10^{-5} SI and therefore rather would belong to the ilmenite series instead of the magnetite series. This is, however, inconsistent with our observations, as the shocked granitoid shows large, fractured magnetite grains. From petrographic observations, one would expect significantly higher magnetic susceptibility because the rock clearly belongs to the magnetite-series granitoids. Therefore, we compared our results with another magnetite-bearing granite for which a hydrothermal breakdown from magnetite to hematite was investigated in detail (Just et al., 2004; Just and Kontny, 2012). Two different stages of alteration were described in the Carboniferous Soultz-sous-Forêts granite in France: Stage I comprised a widespread, synemplacement alteration, the main effect of

which was the localized formation of hematite. The corresponding k - T curves show a clear irreversibility of pure magnetite and positive alteration indexes with the new formation of a ferrimagnetic phase during the measurement in an argon atmosphere. Stage II occurs in fault zones of altered and fresh granite and is characterized by a nearly complete breakdown of magnetite to hematite. This transformation is very prominently seen in the magnetic susceptibility, which significantly decreases in these zones (see fig. 2 in Just and Kontny, 2012). This, again, is clearly distinct from the granitoid basement of the Chicxulub peak ring, where magnetite shows a microscopically visible transformation into hematite, but not a complete breakdown (Fig. 4B). Magnetic susceptibility values range between 50×10^{-5} and 300×10^{-5} SI, which is significantly lower than values of the fresh and stage I granite from Soultz-sous-Forêts, showing magnetic susceptibility values in the order of 1000 – 3000×10^{-5} SI, i.e., one order of magnitude higher than in the peak-ring granitoid rocks. Our peak-ring samples are more in line with the susceptibilities from the stage II Soultz-sous-Forêts granite (~ 50 – 150×10^{-5} SI); however, we do not see comparable levels of oxidation in the peak-ring material. Therefore, we have to assume that either the amount of magnetite during original crystallization was significantly lower, or a shock effect must have been responsible for the significantly lower magnetic susceptibility. Magnetite grains several hundred micrometers in size (Figs. 4A and 4B), even if partially oxidized to hematite, would constitute well above >0.1 wt% of the basement composition, which would still result in magnetic susceptibility values larger than 300×10^{-5} SI units (see fig. 2.1 in Tarling and Hrouda [1993], where a susceptibility range of 50 – 300×10^{-5} SI units requires magnetite to comprise only 0.01–0.1 wt% of the basement). Even relatively low shock pressures (3–5 GPa) can decrease susceptibility by ~90% (Reznik et al., 2016; Kontny and Grothaus, 2017). The peak-ring lithologies experienced shock pressures in the order of 10–35 GPa (Morgan et al., 2017; Ferrière et al., 2017) and clearly were affected by a reduction of magnetic susceptibility. A 90% reduction would lead to original susceptibilities of up to $\sim 1000 \times 10^{-5}$ SI (not considering variation due to an inhomogeneous distribution of magnetite in the granite). This is in the range of the fresh Soultz-sous-Forêts granite in the Upper Rhine graben and other ferrimagnetic Carboniferous granites from the Variscides in Europe and elsewhere (e.g., Henry, 1988; Bouchez and Gleizes, 1995; Bouchez, 1997; Ishihara, 1979; Ishihara et al., 2000; Henry et al., 2004).

Implications for Magnetic Sources of the Chicxulub Impact Structure

Magnetic signatures of complex terrestrial impact craters vary greatly with composition of the target rock, impact-related magnetization, and effects of crater fill and postimpact sedimentation (Pilkington and Grieve, 1992). For the Chicxulub impact crater, three major magnetic sources have been reported for the concentric magnetic anomaly rings (Fig. 1B; Rebolledo-Vieyra et al., 2010): (1) melt rock units, (2) suevite-like breccia, and (3) central uplift with highly magnetized breccia sequences and melt sheets. It is also well known that strong positive magnetic anomalies occur when basement rocks are involved (Pilkington and Grieve, 1992). On the other hand, it is well documented that shock causes a reduction of magnetic susceptibility and often also of remanent magnetization (e.g., Acuña et al., 1999; Plado et al., 1999; Pilkington and Hildebrand, 2000; Ugalde et al., 2005; Bezaeva et al., 2016).

The M0077A core was drilled into a negative magnetic anomaly within the peak ring of the Chicxulub impact crater. Rebolledo-Vieyra et al. (2010) has related the negative magnetic anomaly pattern to a system of regional vertical faults, and the IODP-ICDP Expedition 364 drill core M0077A has revealed that these structures consist of strongly fractured and faulted granitoid rocks (Morgan et al., 2017; Riller et al., 2018). The shock demagnetized the basement granitoid, or at least reduced remanent magnetization and likely randomized the NRM vectors in the basement granitoid, while the remanent magnetization is stronger in the unshocked cation-substituted magnetite formed in the impact melts. The Q ratios reflect this, but even where the Q ratios are above 1 (in the lower impact melt unit melt rock), they are not higher than 3. This observation suggests that the negative magnetic anomalies in the peak ring are dominated by the reduced induced magnetization component of the uplifted and shocked granitoid basement. In the peak ring, the influence of the impact melts with higher susceptibility is negligible, due to their minor thickness (~26 m), when compared to the uplifted basement, which has a thickness of at least 550 m (Fig. 2). The impact melt is suggested to be responsible for the positive magnetic anomaly regions, such as the central basin of the crater (e.g., Rebolledo-Vieyra et al., 2010; Urrutia Fucugauchi et al., 2011), where it likely shows a similar NRM, but susceptibility is more important.

CONCLUSIONS

The IODP-ICDP Expedition 364 drill core M0077A revealed that the Chicxulub peak ring

consists of uplifted granitoid basement rocks overlain by a 130-m-thick impact melt and suevite layer. Pre- and postimpact hydrothermal systems affected this basement with maximum temperatures up to 450 °C. We investigated the rock magnetic properties and magnetic mineralogy in order to study magnetic mineral transformation during pre-, syn-, and postimpact processes. The shock from the impact induced lattice defects and fractures in magnetite, which are responsible for demagnetization and a substantial decrease in magnetic susceptibility. Our results suggest that decreased magnetic susceptibility and magnetization in shocked magnetite from the granitoid basement are responsible for the magnetic anomaly low in the peak ring. In the melt rocks, cation-substituted magnetite records the induced and remanent magnetization, and it acquired a TRM with the expected directions for chron 29r at the time of the impact (Dec/Inc = 180°/−40°), in agreement with earlier studies (Gulick et al., 2019). The postimpact hydrothermal overprint on the shocked magnetite from the basement of the Chicxulub peak ring is negligible from a magnetic properties point of view.

Most of the basement granitoid shows varying degrees of pre-impact oxidation of magnetite. In the basement, the postimpact hydrothermal activity does not visibly contribute to changes in the chemical properties of magnetite, and we only locally observed a transformation of hematite to magnetite due to the reducing character of the hydrothermal fluids, or due to high temperatures near the impact melt. This transformation created new small magnetic grains within the original large grains. The high surface area would be expected to be more prone to oxidation due to seawater percolation at any point after the hydrothermal system ceased. However, we found no clear indication for maghemitization.

The temperature onset of a possible hematite to magnetite transformation is found in *k-T* curves above 580 °C, which is substantially higher than the upper bound of the hydrothermal system's temperature (~450 °C). Our experiments further suggest that the hydrothermal system also did not reach high enough temperatures to anneal the magnetite crystal lattice defects, which we suggest to occur between 540 °C and 560 °C. Therefore, high-temperature overprints in the peak-ring basement are limited to areas in close proximity to and in contact with the impact melt rocks.

ACKNOWLEDGMENTS

The authors would like to thank Sean Gulick, Joanna Morgan, and Michelle Penkrot for their assistance in the sampling process. B.D.L. Mendes would like to thank Ruben Winstel for assistance in the laboratory. This work was funded by the German Research

Foundation, project number 432762445, and partially supported by the National Science Centre (NCN), Poland, in the frame of scientific project no. 2019/03/X/ST10/00139. We acknowledge the thorough reviews by Daniel R. Franco and three anonymous reviewers.

REFERENCES CITED

- Acuña, M.H., et al., 1999, Global distribution of crustal magnetization discovered by the Mars Global Surveyor MAG/ER Experiment: *Science*, v. 284, no. 5415, p. 4753–4771, <https://doi.org/10.1126/science.284.5415.4753>.
- Aragón, R., Buttrey, D.J., Shepherd, J.P., and Honig, J.M., 1985, Influence of nonstoichiometry on the Verwey transition: *Physical Review B*, v. 31, p. 430, <https://doi.org/10.1103/PhysRevB.31.430>.
- Bezaeva, N.S., et al., 2016, The effects of 10 to >160 GPa shock on the magnetic properties of basalt and diabase: *Geochemistry, Geophysics, Geosystems*, v. 17, p. 4753–4771, <https://doi.org/10.1002/2016GC006583>.
- Bialo, I., Kozłowski, A., Wack, M., Włodek, A., Gondek, Ł., Kakol, Z., Hochleitner, R., Zywczak, A., Chlan, V., and Gilder, S.A., 2019, The influence of strain on the Verwey transition as a function of dopant concentration: Towards a geobarometer for magnetite-bearing rocks: *Geophysical Journal International*, v. 219, p. 148–158, <https://doi.org/10.1093/gji/ggz274>.
- Bouchez, J.L., 1997, Granite is never isotropic: An introduction to AMS studies of granitic rocks, in Bouchez, J.L., Hutton, D.H.W., and Stephens, W.E., eds., *Granite: From Segregation of Melt to Emplacement Fabrics*: Dordrecht, Netherlands, Springer, Petrology and Structural Geology Volume 8, p. 95–112, https://doi.org/10.1007/978-94-017-1717-5_6.
- Bouchez, J.L., and Gleizes, G., 1995, Two-stage deformation of the Mont-Louis-Andorra granite pluton (Variscan Pyrenees) inferred from magnetic susceptibility anisotropy: *Journal of the Geological Society*, v. 152, p. 669–679, <https://doi.org/10.1144/gsjgs.152.4.0669>.
- Bowles, J.A., Jackson, M.J., Berquó, T.S., Sölheid, P.A., and Gee, J.S., 2013, Inferred time- and temperature-dependent cation ordering in natural titanomagnetites: *Nature Communications*, v. 4, 1916, p. 1–9, <https://doi.org/10.1038/ncomms2938>.
- Bowles, J.A., Gerzich, D.M., and Jackson, M.J., 2018, Assessing new and old methods in paleomagnetic paleothermometry: A test case at Mt. St. Helens, USA: *Geochemistry, Geophysics, Geosystems*, v. 19, p. 1714–1730, <https://doi.org/10.1029/2018GC007435>.
- Bowles, J.A., Lappe, S.C.L.L., Jackson, M.J., Arenholz, E., and van der Laan, G., 2019, Curie temperature enhancement and cation ordering in titanomagnetites: Evidence from magnetic properties, XMCD, and Mössbauer spectroscopy: *Geochemistry, Geophysics, Geosystems*, v. 20, p. 2272–2289, <https://doi.org/10.1029/2019GC008217>.
- Burgess, S., 2019, Deciphering mass extinction triggers: *Science*, v. 363, no. 6429, p. 815–816, <https://doi.org/10.1126/science.aaw0473>.
- Carporzen, L., and Gilder, S.A., 2010, Strain memory of the Verwey transition: *Journal of Geophysical Research: Solid Earth*, v. 115, no. B5, <https://doi.org/10.1029/2009jb006813>.
- Chadima, M., and Hroudá, H., 2007, Remasoft 3.0 Paleomagnetic Data Browser and Analyzer User Manual: Brno, Czech Republic, AGICO, www.agico.com (accessed April 2022).
- Collins, G.S., et al., 2020, A steeply-inclined trajectory for the Chicxulub impact: *Nature Communications*, v. 11, 1480, p. 1–10, <https://doi.org/10.1038/s41467-020-15269-x>.
- Day, R., Fuller, M., and Schmidt, V.A., 1977, Hysteresis properties of titanomagnetites: Grain-size and compositional dependence: *Physics of the Earth and Planetary Interiors*, v. 13, p. 260–267, [https://doi.org/10.1016/0031-9201\(77\)90108-X](https://doi.org/10.1016/0031-9201(77)90108-X).
- de Graaff, S.J., et al., 2022, New insights into the formation and emplacement of impact melt rocks within the Chicxulub impact structure, following the 2016 IODP-ICDP Expedition 364: *Geological Society of America Bulletin*, v. 134, no. 1–2, p. 293–315, <https://doi.org/10.1130/B35795.1>.
- Dudzisz, K., Kontny, A., and Alva-Valdivia, L.M., 2022, Curie temperatures and emplacement conditions of pyroclastic deposits from Popocatepetl volcano, Mexico: *Geochemistry, Geophysics, Geosystems*, v. 23, <https://doi.org/10.1029/2022GC010340>.
- Dunlop, D.J., 2002, Theory and application of the Day plot (Mrs/Ms versus Hcr/Hc) 1. Theoretical curves and tests using titanomagnetite data: *Journal of Geophysical Research: Solid Earth*, v. 107, <https://doi.org/10.1029/2001JB000486>.
- Dunlop, D.J., 2014, High-temperature susceptibility of magnetite: A new pseudo-single-domain effect: *Geophysical Journal International*, v. 199, p. 707–716, <https://doi.org/10.1093/gji/ggu247>.
- Ebel, D.S., and Grossman, L., 2005, Spinel-bearing spherules condensed from the Chicxulub impact vapor plume: *Geology*, v. 33, no. 4, p. 293–296, <https://doi.org/10.1130/G21136.1>.
- Egli, R., 2013, VARIFORC: An optimized protocol for calculating non-regular first-order reversal curve (FORC) diagrams: *Global and Planetary Change*, v. 110, p. 302–320, <https://doi.org/10.1016/j.gloplacha.2013.08.003>.
- Engelmann, R., 2008, Bestimmung diagnostischer magnetischer Übergangstemperaturen von synthetischen Titanomagnetiten und Ilmenit-Hämatit-Mischkristallen [Ph.D. dissertation]: Heidelberg, Germany, Universität Heidelberg, 285 p., <https://doi.org/10.11588/HEIDOK.00008392>.
- Feignon, J.G., de Graaff, S.J., Ferrière, L., Kaskes, P., Déhais, T., Goderis, S., Claeys, P., and Koeberl, C., 2021, Chicxulub impact structure, IODP-ICDP Expedition 364 drill core: *Geochemistry of the granite basement: Meteoritics & Planetary Science*, v. 56, p. 1243–1273, <https://doi.org/10.1111/maps.13705>.
- Ferrière, L., Rae, A.S.P., Poelchau, M., and Koeberl, C., 2017, Macro- and microscopic evidence of impact metamorphism in rocks from the Chicxulub peak ring, IODP-ICDP Expedition 364 drill core, in 48th Lunar and Planetary Science Conference, held 20–24 March 2017, at The Woodlands, Texas: *Lunar and Planetary Institute Contribution 1964*, abstract 1600.
- Gao, X., et al., 2019, New high-temperature dependence of magnetic susceptibility-based climofunction for quantifying paleoprecipitation from Chinese loess: *Geochemistry, Geophysics, Geosystems*, v. 20, p. 4273–4291, <https://doi.org/10.1029/2019GC008401>.
- Gulick, S., et al., 2017a, Expedition 364 summary, in Morgan, J., Gulick, S., Mellett, C.L., Green, S.L., and the Expedition 364 Scientists, eds., *Chicxulub: Drilling the K-Pg Impact Crater: Proceedings of the International Ocean Discovery Program, Volume 364: College Station, Texas, International Ocean Discovery Program*, <https://doi.org/10.14379/iodp.proc.364.101.2017>.
- Gulick, S., et al., 2017b, Site M0077A: Upper peak ring, in Morgan, J., Gulick, S., Mellett, C.L., Green, S.L., and the Expedition 364 Scientists, eds., *Chicxulub: Drilling the K-Pg Impact Crater: Proceedings of the International Ocean Discovery Program, Volume 364: College Station, Texas, International Ocean Discovery Program*, <https://doi.org/10.14379/iodp.proc.364.106.2017>.
- Gulick, S.P.S., et al., 2008, Importance of pre-impact crustal structure for the asymmetry of the Chicxulub impact crater: *Nature Geoscience*, v. 1, p. 131–135, <https://doi.org/10.1038/ngeo103>.
- Gulick, S.P.S., Christeson, G.L., Barton, P.J., Grieve, R.A.F., Morgan, J.V., and Urrutia-Fucugauchi, J., 2013, Geophysical characterization of the Chicxulub impact crater: *Reviews of Geophysics*, v. 51, p. 31–52, <https://doi.org/10.1002/rog.20007>.
- Gulick, S.P.S., et al., 2019, The first day of the Cenozoic: Proceedings of the National Academy of Sciences of the United States of America, v. 116, p. 19342–19351, <https://doi.org/10.1073/pnas.1909479116>.
- Harrison, R.J., and Feinberg, J.M., 2008, FORCinel: An improved algorithm for calculating first-order reversal curve distributions using locally weighted regression smoothing: *Geochemistry, Geophysics, Geosystems*, v. 9, no. 5, <https://doi.org/10.1029/2008GC001987>.
- Harrison, R.J., and Putnis, A., 1998, The magnetic properties and crystal chemistry of oxide spinel solid solutions:

- Surveys in Geophysics, v. 19, p. 461–520, <https://doi.org/10.1023/A:1006535023784>.
- Harrison, R.J., and Putnis, A., 1999, Determination of the mechanism of cation ordering in magnesioferrite (Mg-Fe₂O₄) from the time- and temperature-dependence of magnetic susceptibility: *Physics and Chemistry of Minerals*, v. 26, p. 322–332, <https://doi.org/10.1007/s002690050192>.
- Henry, B., 1988, The magnetic fabrics of the Egletons granite (France): Separation and structural implications: *Physics of the Earth and Planetary Interiors*, v. 51, p. 253–263, [https://doi.org/10.1016/0031-9201\(88\)90067-2](https://doi.org/10.1016/0031-9201(88)90067-2).
- Henry, B., Djellit, H., Bayou, B., Derder, M.E.M., Ouabadi, A., Merahi, M.K., Baziz, K., Khaldi, A., and Hemmi, A., 2004, Emplacement and fabric-forming conditions of the Arous-En-Tides granite, eastern border of the Tin Seririne/Tin Mersoi basin (Algeria): Magnetic and visible fabrics analysis: *Journal of Structural Geology*, v. 26, p. 1647–1657, <https://doi.org/10.1016/j.jsg.2004.02.003>.
- Hildebrand, A., Penfield, G., Kring, D., Mark, P., Camarago, A., Jacobsen, S., and Boynton, W., 1991, Chicxulub crater: A possible Cretaceous/Tertiary boundary impact crater on the Yucatán Peninsula, Mexico: *Geology*, v. 19, no. 9, p. 867–871, [https://doi.org/10.1130/0091-7613\(1991\)019<0867:CCAPCT>2.3.CO;2](https://doi.org/10.1130/0091-7613(1991)019<0867:CCAPCT>2.3.CO;2).
- Hrouda, F., 2003, Indices for numerical characterization of the alteration processes of magnetic minerals taking place during investigation of temperature variation of magnetic susceptibility: *Studia Geophysica et Geodaetica*, v. 47, p. 847–861, <https://doi.org/10.1023/A:1026398920172>.
- Ishihara, S., 1979, Lateral variation of magnetic susceptibility of the Japanese granitoids: *Journal of the Geological Society of Japan (Chishitsugaku Zasshi)*, v. 85, p. 509–523, <https://doi.org/10.5575/geosoc.85.509>.
- Ishihara, S., Hashimoto, M., and Machida, M., 2000, Magnetite/ilmenite-series classification and magnetic susceptibility of the Mesozoic–Cenozoic batholiths in Peru: *Resource Geology*, v. 50, p. 123–129, <https://doi.org/10.1111/j.1751-3928.2000.tb00062.x>.
- Jackson, M., and Bowles, J.A., 2014, Curie temperatures of titanomagnetite in ignimbrites: Effects of emplacement temperatures, cooling rates, exsolution, and cation ordering: *Geochemistry, Geophysics, Geosystems*, v. 15, p. 4343–4368, <https://doi.org/10.1002/2014GC005527>.
- Just, J., and Kontny, A., 2012, Thermally induced alterations of minerals during measurements of the temperature dependence of magnetic susceptibility: A case study from the hydrothermally altered Soultz-sous-Forêts granite, France: *International Journal of Earth Sciences*, v. 101, p. 819–839, <https://doi.org/10.1007/s00531-011-0668-9>.
- Just, J., Kontny, A., de Wall, H., Hirt, A.M., and Martín-Hernández, F., 2004, Development of magnetic fabrics during hydrothermal alteration in the Soultz-sous-Forêts granite from the EPS-1 borehole, Upper Rhine graben, in Martín-Hernández, F., Lüneberg, C.M., Aubourg, C., and Jackson, M., eds., *Magnetic Fabric: Methods and Applications*: Geological Society, London, Special Publication 238, p. 509–526, <https://doi.org/10.1144/GSL.SP.2004.238.01.26>.
- Keppie, J.D., Dostal, J., Norman, M., Urrutia-Fucuguchi, J., and Grajales-Nishimura, M., 2011, Study of melt and a clast of 546 Ma magmatic arc rocks in the 65 Ma Chicxulub bolide breccia, northern Maya block, Mexico: Western limit of Eidiacaran arc peripheral to northern Gondwana: *International Geology Review*, v. 53, p. 1180–1193, <https://doi.org/10.1080/00206810903545527>.
- Kirschvink, J.L., 1980, The least-squares line and plane and the analysis of palaeomagnetic data: *Geophysical Journal International*, v. 62, p. 699–718, <https://doi.org/10.1111/j.1365-246X.1980.tb02601.x>.
- Kontny, A., and Grothaus, L., 2017, Effects of shock pressure and temperature on titanomagnetite from ICDP cores and target rocks of the El'gygytgyn impact structure, Russia: *Studia Geophysica et Geodaetica*, v. 61, p. 162–183, <https://doi.org/10.1007/s12200-016-0819-3>.
- Kontny, A., Reznik, B., Boubnov, A., Göttlicher, J., and Steininger, R., 2018, Postshock thermally induced transformations in experimentally shocked magnetite: *Geochemistry, Geophysics, Geosystems*, v. 19, p. 921–931, <https://doi.org/10.1002/2017GC007331>.
- Koymans, M.R., Langereis, C.G., Pastor-Galán, D., and van Hinsbergen, D.J.J., 2016, Paleomagnetism.org: An online multi-platform open source environment for paleomagnetic data analysis: *Computers & Geosciences*, v. 93, p. 127–137, <https://doi.org/10.1016/j.cageo.2016.05.007>.
- Koymans, M.R., van Hinsbergen, D.J.J., Pastor-Galán, D., Vaes, B., and Langereis, C.G., 2020, Towards FAIR paleomagnetic data management through Paleomagnetism.org 2.0: *Geochemistry, Geophysics, Geosystems*, v. 21, <https://doi.org/10.1029/2019GC008838>.
- Kring, D., Claeys, P., Gulick, S., Morgan, J., and Gareth, C., 2017, Chicxulub and the exploration of large peak-ring impact craters through scientific drilling: *GSA Today*, v. 27, no. 10, p. 4–8, <https://doi.org/10.1130/GSATG352A.1>.
- Kring, D.A., et al., 2020, Probing the hydrothermal system of the Chicxulub impact crater: *Science Advances*, v. 6, p. 3053–3082, <https://doi.org/10.1126/sciadv.aaz3053>.
- Kruiver, P.P., Dekkers, M.J., and Heslop, D., 2001, Quantification of magnetic coercivity components by the analysis of acquisition curves of isothermal remanent magnetisation: *Earth and Planetary Science Letters*, v. 189, p. 269–276, [https://doi.org/10.1016/S0012-821X\(01\)00367-3](https://doi.org/10.1016/S0012-821X(01)00367-3).
- Lagoeiro, L.E., 1998, Transformation of magnetite to hematite and its influence on the dissolution of iron oxide minerals: *Journal of Metamorphic Geology*, v. 16, p. 415–423, <https://doi.org/10.1111/j.1525-1314.1998.00144.x>.
- Lanci, L., and Kent, D.V., 2003, Introduction of thermal activation in forward modeling of hysteresis loops for single-domain magnetic particles and implications for the interpretation of the Day diagram: *Journal of Geophysical Research: Solid Earth*, v. 108, 2142, <https://doi.org/10.1029/2001JB000944>.
- Lattard, D., Engelmann, R., Kontny, A., and Sauerzapf, U., 2006, Curie temperatures of synthetic titanomagnetites in the Fe-Ti-O system: Effects of composition, crystal chemistry, and thermomagnetic methods: *Journal of Geophysical Research*, v. 111, no. B12, <https://doi.org/10.1029/2006JB004591>.
- Lied, P., Kontny, A., Nowaczyk, N., Mrlina, J., and Kämpf, H., 2020, Cooling rates of pyroclastic deposits inferred from mineral magnetic investigations: A case study from the Pleistocene Mýtina Maar (Czech Republic): *International Journal of Earth Sciences*, v. 109, p. 1707–1725, <https://doi.org/10.1007/s00531-020-01865-1>.
- Lindquist, A.K., Feinberg, J.M., Harrison, R.J., Loudon, J.C., and Newell, A.J., 2015, Domain wall pinning and dislocations: Investigating magnetite deformed under conditions analogous to nature using transmission electron microscopy: *Journal of Geophysical Research: Solid Earth*, v. 120, p. 1415–1430, <https://doi.org/10.1002/2014JB011335>.
- Louzada, K.L., Stewart, S.T., Weiss, B.P., Gattacceca, J., and Bezaeva, N.S., 2010, Shock and static pressure demagnetization of pyrrhotite and implications for the Martian crust: *Earth and Planetary Science Letters*, v. 290, p. 90–101, <https://doi.org/10.1016/j.epsl.2009.12.006>.
- Mang, C., and Kontny, A., 2013, Origin of two Verwey transitions in different generations of magnetite from the Chesapeake Bay impact structure, USA: *Journal of Geophysical Research: Solid Earth*, v. 118, p. 5195–5207, <https://doi.org/10.1002/jgrb.50291>.
- Mang, C., Kontny, A., Fritz, J., and Schneider, R., 2013, Shock experiments up to 30 GPa and their consequences on microstructures and magnetic properties in pyrrhotite: *Geochemistry, Geophysics, Geosystems*, v. 14, p. 64–85, <https://doi.org/10.1029/2012GC004242>.
- McCall, N., et al., 2017, Adjustments and preliminary analysis of Chicxulub peak ring CT scans: Lunar and Planetary Science Conference XXCVII, poster 1522, <https://www.hou.usra.edu/meetings/lpsc2017/pdf/1522.pdf>.
- McFadden, P.L., and McElhinny, M.W., 1988, The combined analysis of remagnetization circles and direct observations in palaeomagnetism: *Earth and Planetary Science Letters*, v. 87, p. 161–172, [https://doi.org/10.1016/0012-821X\(88\)90072-6](https://doi.org/10.1016/0012-821X(88)90072-6).
- Mi, W.B., Jiang, E.Y., and Bai, H.L., 2009, Fe³⁺/Fe²⁺ ratio controlled magnetic and electrical transport properties of polycrystalline Fe_{3(1-δ)}O₄ films: *Journal of Physics D: Applied Physics*, v. 42, <https://doi.org/10.1088/0022-3727/42/10/105007>.
- Morgan, J., and Artemieva, N., 2008, Chicxulub distal ejecta: Modeling versus observations, in Morgan, J., and Artemieva, N., eds., *Large Meteorite Impacts and Planetary Evolution IV, Vredefort Dome, South Africa: Lunar and Planetary Institute Contribution 1423*, paper ID 3016, <https://ui.adsabs.harvard.edu/abs/2008LPICo1423.3016M/abstract> (accessed April 2022).
- Morgan, J., et al., 1997, Size and morphology of the Chicxulub impact crater: *Nature*, v. 390, p. 472–476, <https://doi.org/10.1038/37291>.
- Morgan, J., Gulick, S., Mellett, C.L., and Green, S.L., 2017, Chicxulub: Drilling the K-Pg impact crater, in Morgan, J., Gulick, S., Mellett, C.L., Green, S.L., and the Expedition 364 Scientists, eds., *Chicxulub: Drilling the K-Pg Impact Crater: Proceedings of the International Ocean Discovery Program, Volume 364: College Station, Texas, International Ocean Discovery Program*, <https://doi.org/10.14379/iodp.proc.364.2017>.
- Morgan, J.V., Warner, M.R., Collins, G.S., Melosh, H.J., and Christeson, G.L., 2000, Peak-ring formation in large impact craters: Geophysical constraints from Chicxulub: *Earth and Planetary Science Letters*, v. 183, p. 347–354, [https://doi.org/10.1016/S0012-821X\(00\)00307-1](https://doi.org/10.1016/S0012-821X(00)00307-1).
- Mullender, T.A.T., van Velzen, A.J., and Dekkers, M.J., 1993, Continuous drift correction and separate identification of ferrimagnetic and paramagnetic contributions in thermomagnetic runs: *Geophysical Journal International*, v. 114, p. 663–672, <https://doi.org/10.1111/j.1365-246X.1993.tb06995.x>.
- Nishitani, T., and Kono, M., 1981, Grain size effect on the low-temperature oxidation of titanomagnetite: *Journal of Geophysics*, v. 50, p. 137–142, <https://journal-geophysicsjournal.com/JoG/article/view/266#nav-menu>.
- O'Reilly, W., 1984, Magnetic properties of titanomagnetites and titanomaghemites, in O'Reilly, W., Rock and Mineral Magnetism: Boston, Massachusetts, Springer US, p. 132–171, https://doi.org/10.1007/978-1-4684-8468-7_7.
- Osinski, G.R., et al., 2020, Explosive interaction of impact melt and seawater following the Chicxulub impact event: *Geology*, v. 48, no. 2, p. 108–112, <https://doi.org/10.1130/G46783.1>.
- Özdemir, Ö., and Dunlop, D.J., 1997, Effect of crystal defects and internal stress on the domain structure and magnetic properties of magnetite: *Journal of Geophysical Research: Solid Earth*, v. 102, p. 20,211–20,224, <https://doi.org/10.1029/97JB01779>.
- Özdemir, Ö., and Dunlop, D.J., 2010, Hallmarks of magnetization in low-temperature remanence cycling of partially oxidized magnetite nanoparticles: *Journal of Geophysical Research: Solid Earth*, v. 115, no. B2, <https://doi.org/10.1029/2009JB006756>.
- Özdemir, Ö., Dunlop, D.J., and Moskowitz, B.M., 1993, The effect of oxidation on the Verwey transition in magnetite: *Geophysical Research Letters*, v. 20, p. 1671–1674, <https://doi.org/10.1029/93GL01483>.
- Penfield, G.T., and Camargo, A., 1981, Definition of a major igneous zone in the central Yucatán platform with aeromagnetics and gravity [abs.], in 51st Annual Meeting of the Society of Exploration Geophysicists: Tulsa, Oklahoma, Society of Exploration Geophysicists, p. 37.
- Petrovský, E.D., and Kapička, A., 2006, On determination of the Curie point from thermomagnetic curves: *Journal of Geophysical Research: Solid Earth*, v. 111, no. B12, B12S27, <https://doi.org/10.1029/2006JB004507>.
- Pilkington, M., and Grieve, R.A.F., 1992, The geophysical signature of terrestrial impact craters: *Reviews of Geophysics*, v. 30, p. 161–181, <https://doi.org/10.1029/92RG00192>.
- Pilkington, M., and Hildebrand, A.R., 2000, Three-dimensional magnetic imaging of the Chicxulub crater: *Journal of Geophysical Research: Solid Earth*, v. 105, p. 23,479–23,491, <https://doi.org/10.1029/2000JB900222>.
- Pilkington, M., Ames, D.E., and Hildebrand, A.R., 2004, Magnetic mineralogy of the Yaxcopoil-1 core, Chicxulub: Meteoritics & Planetary Science, v. 39, p. 831–841, <https://doi.org/10.1111/j.1945-5100.2004.tb00933.x>.

- Plado, J., Pesonen, L., and Puura, V., 1999, Effect of erosion on gravity and magnetic signatures of complex impact structures: Geophysical modeling and applications, *in* Dressler, B.O., and Sharpton, V.L., eds., *Large Meteorite Impacts and Planetary Evolution II: Geological Society of America Special Paper 339*, p. 229–240, <https://doi.org/10.1130/0-8137-2339-6.229>.
- Ramos, E.L., 1975, Geological summary of the Yucatan Peninsula, *in* Nairn, A.E.M., and Stehli, F.G., eds., *The Gulf of Mexico and the Caribbean*: Boston, Massachusetts, Springer, p. 257–282, https://doi.org/10.1007/978-1-4684-8535-6_7.
- Rasmussen, C., Stockli, D.F., Ross, C.H., Pickersgill, A., Gulick, S.P., Schmieder, M., Christeson, G.L., Wittmann, A., Kring, D.A., and Morgan, J.v., 2019, U-Pb memory behavior in Chicxulub's peak ring—Applying U-Pb depth profiling to shocked zircon: *Chemical Geology*, v. 525, p. 356–367, <https://doi.org/10.1016/j.chemgeo.2019.07.029>.
- Rebolledo-Vieyra, M., Urrutia-Fucugauchi, J., and López-Loera, H., 2010, Aeromagnetic anomalies and structural model of the Chicxulub multiring impact crater, Yucatan, Mexico: *Revista Mexicana de Ciencias Geológicas*, v. 27, p. 185–195, http://www.scielo.org.mx/scielo.php?pid=S1026-87742010000100016&script=sci_arttext&tlng=en (accessed April 2022).
- Renne, P., 2013, Synchrony between the Chicxulub impact and the Cretaceous-Paleogene boundary extinctions: What does it mean?: Washington, D.C., American Geophysical Union, Spring Meeting, <https://ui.adsabs.harvard.edu/abs/2013AGUSM.U34B.04R/abstract> (accessed April 2022).
- Reznik, B., Kontny, A., Fritz, J., and Gerhards, U., 2016, Shock-induced deformation phenomena in magnetite and their consequences on magnetic properties: *Geochemistry, Geophysics, Geosystems*, v. 17, p. 2374–2393, <https://doi.org/10.1002/2016GC006338>.
- Riller, U., et al., 2018, Rock fluidization during peak-ring formation of large impact structures: *Nature*, v. 562, p. 511–518, <https://doi.org/10.1038/s41586-018-0607-z>.
- Roberts, A.P., Heslop, D., Zhao, X., and Pike, C.R., 2014, Understanding fine magnetic particle systems through use of first-order reversal curve diagrams: *Reviews of Geophysics*, v. 52, p. 557–602, <https://doi.org/10.1002/2014RG000462>.
- Roberts, A.P., Tauxe, L., Heslop, D., Zhao, X., and Jiang, Z., 2018, A critical appraisal of the “Day” diagram: *Journal of Geophysical Research: Solid Earth*, v. 123, p. 2618–2644, <https://doi.org/10.1002/2017JB015247>.
- Ross, C.H., et al., 2022, Evidence of Carboniferous arc magmatism preserved in the Chicxulub impact structure: *Geological Society of America Bulletin*, v. 134, no. 1–2, p. 241–260, <https://doi.org/10.1130/B35831.1>.
- Schulte, P., et al., 2010, The Chicxulub asteroid impact and mass extinction at the Cretaceous-Paleogene boundary: *Science*, v. 327, no. 5970, p. 1214–1218, <https://doi.org/10.1126/science.1177265>.
- Sharpton, V.L., Brent Dalrymple, G., Marin, L.E., Ryder, G., Schuraytz, B.C., and Urrutia-Fucugauchi, J., 1992, New links between the Chicxulub impact structure and the Cretaceous/Tertiary boundary: *Nature*, v. 359, p. 819–821, <https://doi.org/10.1038/359819a0>.
- Smit, J., 1999, The global stratigraphy of the Cretaceous-Tertiary boundary impact ejecta: *Annual Review of Earth and Planetary Sciences*, v. 27, p. 75–113, <https://doi.org/10.1146/annurev.earth.27.1.75>.
- Tarling, D.H., and Hrouda, F., 1993, *The Magnetic Anisotropy of Rocks*: London, Chapman & Hall, 217 p.
- Tikoo, S., et al., 2017, Paleomagnetic insights into impact-related hydrothermal systems and magnetic anomalies at the Chicxulub crater: Washington, D.C., American Geophysical Union, Fall meeting, abstract P23H-05, <https://ui.adsabs.harvard.edu/abs/2017AGUFM.P23H.05T/abstract> (accessed September 2022).
- Ugalde, H., Artemieva, N., and Milkeriet, B., 2005, Magnetization on impact structures—Constraints from numerical modeling and petrophysics, *in* Kenkmann, T., Hörz, F., and Deutsch, A., eds., *Large Meteorite Impacts III: Geological Society of America Special Paper 384*, p. 25–42, <https://doi.org/10.1130/0-8137-2384-1.25>.
- Urrutia-Fucugauchi, J., Camargo-Zanoguera, A., Pérez-Cruz, L., and Pérez-Cruz, G., 2011, The Chicxulub multiring impact crater, Yucatan carbonate platform, Gulf of Mexico: *Geofísica Internacional*, v. 50, p. 99–127, <https://doi.org/10.22201/igeof.00167169p.2011.50.1.125>.
- Urrutia-Fucugauchi, J., Perez-Cruz, L.L., Tikoo, S., Riller, U.P., Rebolledo-Vieyra, M., Morgan, J.v., and Gulick, S.P.S., 2018, Magnetic fabrics and properties of impactites and basement beneath the peak ring of Chicxulub crater—IODP-ICDP Expedition 364: Washington, D.C., American Geophysical Union, Fall Meeting, abstract PP51D-1165, <https://ui.adsabs.harvard.edu/abs/2018AGUFMPP51D1165F/abstract> (accessed April 2022).
- Vahle, C., Kontny, A., Gunnlaugsson, H.P., and Kristjansson, L., 2007, The Stardalur magnetic anomaly revisited—New insights into a complex cooling and alteration history: *Physics of the Earth and Planetary Interiors*, v. 164, p. 119–141, <https://doi.org/10.1016/j.pepi.2007.06.004>.
- Verwey, E.J.W., 1939, Electronic conduction of magnetite (Fe₃O₄) and its transition point at low temperatures: *Nature*, v. 144, p. 327–328, <https://doi.org/10.1038/144327b0>.
- Weber, B., González-Guzmán, R., Manjarrez-Juárez, R., Cisneros de León, A., Martens, U., Solari, L., Hecht, L., and Valencia, V., 2018, Late Mesoproterozoic to early Paleozoic history of metamorphic basement from the southeastern Chiapas Massif Complex, Mexico, and implications for the evolution of NW Gondwana: *Lithos*, v. 300–301, p. 177–199, <https://doi.org/10.1016/j.lithos.2017.12.009>.
- Witts, J.D., Newton, R.J., Mills, B.J.W., Wignall, P.B., Bottrell, S.H., Hall, J.L.O., Francis, J.E., and Alistair Crame, J., 2018, The impact of the Cretaceous-Paleogene (K-Pg) mass extinction event on the global sulfur cycle: Evidence from Seymour Island, Antarctica: *Geochimica et Cosmochimica Acta*, v. 230, p. 17–45, <https://doi.org/10.1016/j.gca.2018.02.037>.
- Zhang, Q., Appel, E., Stanjek, H., Byrne, J.M., Berthold, C., Sorwat, J., Rösler, W., and Seemann, T., 2020, Humidity related magnetite alteration in an experimental setup: *Geophysical Journal International*, v. 224, p. 69–85, <https://doi.org/10.1093/gji/ggaa394>.
- Zhang, Q., Appel, E., Basavaiah, N., Hu, S., Zhu, X., and Neumann, U., 2021, Is alteration of magnetite during rock weathering climate-dependent?: *Journal of Geophysical Research: Solid Earth*, v. 126, <https://doi.org/10.1029/2021JB022693>.
- Zhao, J., et al., 2020, Geochemistry, geochronology and petrogenesis of Maya block granitoids and dykes from the Chicxulub impact crater, Gulf of México: Implications for the assembly of Pangea: *Gondwana Research*, v. 82, p. 128–150, <https://doi.org/10.1016/j.gr.2019.12.003>.
- Zhao, X., and Liu, Q., 2010, Effects of the grain size distribution on the temperature-dependent magnetic susceptibility of magnetite nanoparticles: *Science China: Earth Sciences*, v. 53, p. 1071–1078, <https://doi.org/10.1007/s11430-010-4015-y>.
- Zijderveld, J.D.A., 1967, The natural remanent magnetizations of the Exeter volcanic traps (Permian, Europe): *Tectonophysics*, v. 4, p. 121–153, [https://doi.org/10.1016/0040-1951\(67\)90048-0](https://doi.org/10.1016/0040-1951(67)90048-0).

SCIENCE EDITOR: WENJIAO XIAO
ASSOCIATE EDITOR: XIXI ZHAO

MANUSCRIPT RECEIVED 19 APRIL 2022
REVISED MANUSCRIPT RECEIVED 17 JANUARY 2023
MANUSCRIPT ACCEPTED 23 FEBRUARY 2023

Printed in the USA